UNIVERSITÀ DEGLI STUDI DI PADOVA
DEPARTMENT OF INFORMATION ENGINEERING
Master Thesis in Telecommunication Engineering

# DESIGN OF REAL-TIME OPTICAL COHERENCE TOMOGRAPHY

*Master Candidate*
GIANLUCA MARCON

*Supervisor*
LUCA PALMIERI

April 18, 2018
Academic Year 2017/2018

UNIVERSITÀ DEGLI STUDI DI PADOVA

DEPARTMENT OF INFORMATION ENGINEERING

Master Thesis in Telecommunication Engineering

# DESIGN OF REAL-TIME OPTICAL COHERENCE TOMOGRAPHY

*Master Candidate*

GIANLUCA MARCON

*Supervisor*

LUCA PALMIERI

April 18, 2018

Academic Year 2017/2018

*If one feels the need of something grand, something infinite, something that makes one feel aware of God, one need not go far to find it. I think that I see something deeper, more infinite, more eternal than the ocean in the expression of the eyes of a little baby when it wakes in the morning and coos or laughs because it sees the sun shining on its cradle.*

---

*Vincent van Gogh*

Dedicated to my niece, Teresa.

*April 2018*

# ABSTRACT

Optical Coherence Tomography (OCT) is a non-invasive imaging technique that exploits the coherence property of light to generate 2-D (cross-sectional) and 3-D (volumetric) images of a live sample from the backscattered electromagnetic field. OCT imaging has found widespread application in medicine, mainly in the areas of *Ophthalmology* and *Angiography*, but also in industrial processes where non-destructive or contactless testing is necessary.

There are two main categories of OCT systems: Time-Domain OCT (TD-OCT) and Fourier-Domain OCT (FD-OCT). As the names suggest, the former technique makes use of time domain measurements, while the latter takes advantage of the frequency contents of the reflected signals. FD-OCT offers significant advantages over TD-OCT, such as faster scanning rates, better imaging resolution, and enhanced sensitivity, while at the same time requiring no mechanical movements of critical components such as lenses or collimators.

In this thesis I focus on a particular FD-OCT technique called Swept-Source OCT (SS-OCT), which uses a rapidly tunable narrow band laser as a light source. A working SS-OCT system capable of real-time imaging is fully developed, along with the data-acquisition and signal-processing modules needed for a complete tomographic imaging device.

Future development includes the migration of the signal processing stack on a Graphics Processing Unit (GPU) in order to enhance the performance of the system making use of the General-Purpose computing on Graphics Processing Units (GPGPU) paradigm. This approach opens up the possibility to implent more advanced and refined OCT schemes, such as Polarization-Sensitive OCT (PS-OCT) and Speckle Variance OCT (svOCT).



# SOMMARIO

La Tomografia a Coerenza Ottica (OCT) è una tecnica di imaging non invasiva che sfrutta la proprietà di coerenza della luce per generare immagini 2-D (a sezioni) e 3-D (volumetriche) di un campione in vivo a partire dalla luce retrodiffusa dallo stesso. La tecnica OCT ha trovato ampio utilizzo nel campo della medicina, in particolare nelle aree dell'*Oftalmologia* e dell'*Angiografia*, ma anche in processi industriali in

cui sono necessarie misure non distruttive e senza contatto.

Vi sono due principali categorie di sistemi OCT: TD-OCT (OCT nel dominio del tempo) e FD-OCT (OCT nel dominio della frequenza). Come suggerisce il nome, la prima di queste due tecniche sfrutta delle misure nel dominio del tempo, mentre la seconda utilizza il contenuto spettrale dei segnali riflessi per ricostruire l'immagine del campione in esame. FD-OCT offre vantaggi significativi rispetto a TD-OCT, come velocità di scansione più elevate, risoluzione più fine e migliore sensitività. Tutto ciò avviene senza che vi siano movimenti meccanici di componenti critici come lenti e collimatori.

In questa tesi lavorerò su un particolare sistema FD-OCT chiamato Swept-Source OCT (SS-OCT) che sfrutta un laser a banda molto stretta e con alta velocità di sintonizzazione. Verrà quindi sviluppato un sistema SS-OCT funzionante, capace di eseguire misure continue e in tempo reale. Il lavorò verterà sulla parte di progettazione e ottimizzazione dello schema ottico e sullo sviluppo di algoritmi per l'acquisizione ed elaborazione dei dati.

Sviluppi futuri verteranno sulla migrazione dell'intero sistema di elaborazione dati su GPU (Graphical Processing Unit) facendo uso del paradigma di General-Purpose computing on Graphics Processing Units (GPGPU), che renderà più efficente il dispositivo e permetterà la progettazione di tecniche più avanzate come OCT sensibile alla polarizzazione (PS-OCT), per ottenere misure di birifrangenza del campione, o Speckle Variance OCT (svOCT).

*In truth, O judges, while I wish to be adorned with every virtue, yet there is nothing which I can esteem more highly than the being and appearing grateful. For this one virtue is not only the greatest, but is also the parent of all the other virtues.*

— Marcus Tullius Cicero

# ACKNOWLEDGEMENTS

First of all, I would like to thank professor Palmieri, my supervisor, for the opportunity he gave me to work on this project, but mostly for his countless advices which made my job a little easier.

A special thought goes to my class mates Giacomo, Linda and Caterina, with which I shared these last few months as a university student, and the other lab-mates Riccardo, Leonardo, Gianluca, Francesco and especially Marco, whom I could always rely upon.

I also thank Elena, who was always by my side in the most difficult moments.

Finally, I heartily thank my family for the essential role they played in my life up until now. Thank you Annachiara, Mariella and Giancarlo.

# CONTENTS

# LIST OF FIGURES

## LIST OF TABLES



## LISTINGS



## ACRONYMS

OCT Optical Coherence Tomography

SS-OCT Swept-Source OCT

TD-OCT Time-Domain OCT

FD-OCT Fourier-Domain OCT

SD-OCT Spectral-Domain OCT

PS-OCT Polarization-Sensitive OCT

svOCT Speckle Variance OCT

GPGPU General-Purpose computing on Graphics Processing Units

GPU Graphics Processing Unit

MZI Mach-Zender interferometer

OPD Optical Path Difference

BPD Balanced Photodiode

OSA Optical Spectrum Analyzer

EOCT Endoscopic Optical Coherence Tomography

IVUS Intravascular Ultrasound

SEM Scanning Electron Microscope

MRI Magnetic Resonance Imaging

DOCT Doppler OCT

PEG Photonic and Electromagnetic Group

DEI Department of Information Engineering

DAQ Data acquisition

PZT piezoelectric transducer

ADC Analog-to-Digital Converter

SLD Superluminescent Diode

CCD charged coupled device

CMOS complementary metal-oxide semiconductor

SNR signal-to-noise ratio

FWHM full-width half-maximum

PSD power spectral density

OFDI optical frequency domain interferometry

MEMS micro electro-mechanical systems

PZT piezoelectric transducer

EOM electro-optic modulator

SOA semiconductor optical amplifier

FDML Fourier domain mode locking

VCSEL vertical cavity surface-emitting laser

# 1 INTRODUCTION

## 1.1 SUMMARY ON OPTICAL COHERENCE TOMOGRAPHY

The technique of Optical Coherence Tomography (OCT), firstly introduced in the late 80's by Fujimoto et al. [19] and later improved by Huang et al. [23], was delevoped for the noninvasive axial and cross-sectional imaging of biological tissues. In a way similar to ultrasonic imaging, 2D images are generated by combining the incident electromagnetic radiation with its delayed version reflected by the sample under test.

The advantage over conventional ultrasound techniques is that it permits imaging resolutions that range from 1 to 20 µm, which is up to two orders of magnitude smaller than for ultrasound. This enables the diagnonis of pathologies which were previously only detectable by histological techniques, which have the advantage of higher resolution at the expense of the capability of non-destructive measurement. In fact, histology requires the following steps to be performed on the sample:

- Excision
- Fixation
- Embedding
- Microtoming
- Staining

These operations prevent the use of histology in certain areas where the sample to be analyzed cannot be damaged, such as *Ophtalmology*, a field of medicine which studies the pathologies of the human eyeball and orbit. These characteristics, coupled with its real-time imaging capability, make OCT one of the strongest candidates for this particular branch of medicine.

In Figure 1.1 we can compare the images of a human retina obtained with the first type of OCT technique invented, Time-Domain OCT (TD-OCT) (Figure 1.1a) and histology (Figure 1.1b) [23]. Image quality, while arguably low, is enough to identify and measure the thickness of the main structures of the eye. In Figure 1.1c we can instead see a high quality image of a live sample obtained with the more modern Swept-Source OCT (SS-OCT) technique [14], which allows higher quality measurements and fast image acquisitions.

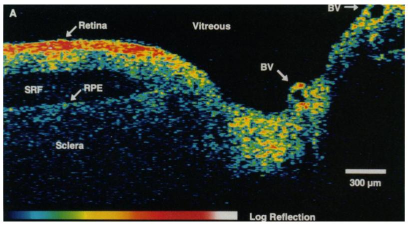


(a) OCT

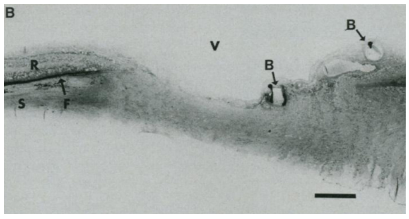


(b) Histology

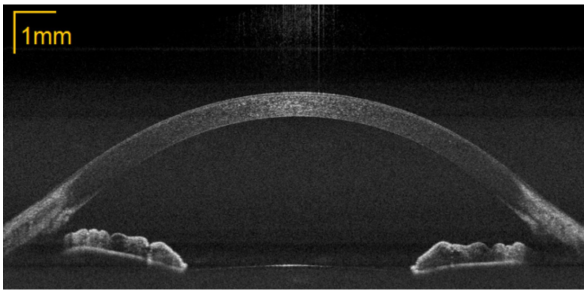


(c) SSOCT

Figure 1.1: Optical coherence tomograph of human retina and optic disk in vitro (top left) and histologic section of the same sample (top right) [23]. On the bottom, a SS-OCT image of a live human eye sample [14].

The first drawback of OCT as a medical imaging technique comes from its relatively low imaging penetration, which is usually between less than a millimeter up to a couple of centimeter, depending on the specific technology and the absorption coefficient of the sample to analyse. In Figure 1.2, a comparison between OCT, Ultrasound, and Confocal Microscopy is available [15]. The trend is that for an increasingly better imaging resolution, imaging depth has to be sacrificed. In this aspect, OCT sits right between the other two techniques, offering micrometer-level resolution for a moderate image penetration.

Whenever cross-sectional images are not sufficient for a correct diagnosis, volumetric data can be exploited for a more in-depth analy-

| SOURCE | YEAR | VOXELS | VOL. RATE | SPEED |
|---|---|---|---|---|
| | | | Volumes/s | GVoxels/s |
| Zhang and Kang[47] | 2010 | 6400000 | 10 | 0.06 |
| Choi et al. [10] | 2012 | 4194304 | 41 | 0.17 |
| Wieser et al. [44] | 2014 | 40960000 | 26 | 1.07 |
| Darbrazi [12] | 2016 | 1408800000 | 2.05 | 2.89 |

Table 1.1: Performance of different implementations of volumetric OCT using GPGPU (adapted from [12]).

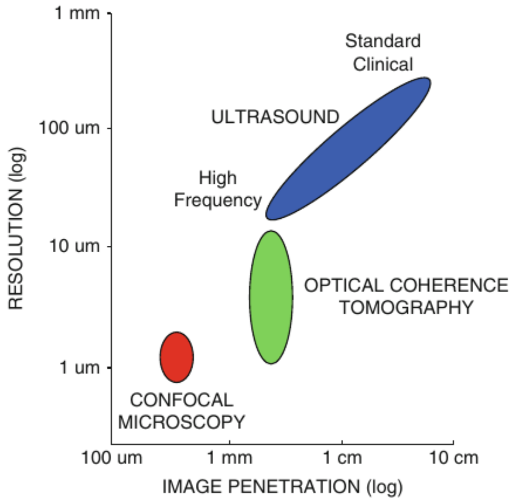


Figure 1.2: Imaging resolution and image penetration compared for different imaging techniques.

sis. Volumetric images are composed by multiple 2D images captured in succession along a certain scanning direction, creating a 3D grid of datapoints called Voxels. . Two examples of 3D-OCT data obtained with SS-OCT (left) [14] and SD-OCT (right) [10] are depicted in Figure 1.3.

*A voxel is the primary unit of three-dimensional datasets, like the pixel is for 2D data. The word voxel originated by analogy with the word "pixel", with vo representing "volume" and el representing "element"*

With the near-exponential growth in computing power over the last decades, and the advent of GPU computing by means of the GPGPU paradigm, advanced volume rendering and signal-processing algorithms can be applied on large OCT data sets in real-time. In Table 1.1 a few results from the literature are summarized, highlighting the advancement in processing power using GPU solutions (adapted from [12]).

Starting from 3D-OCT data it is also possible to generate *en-face* projections of the sample at different depths, providing an invaluable tool for further analysis. A result of this technique is available in Figure 1.4, which shows a frontal view of the macula, the central part of the retina, affected by an edema.

## 1.2 APPLICATIONS

### 1.2.1 *Medicine*

*Angiography or arteriography is a medical imaging technique used to visualize the inside, or lumen, of blood vessels and organs of the body*

Ophtalmic applications have already been briefly mentioned in Section 1.1, but other areas of medicine such as Cardiology [7, 24] and Angiography [25, 39] have benefitted from the diagnostic capabilities of OCT. A comparison between OCT and Ultrasound images of a coronary plaque is available in Figure 1.5: the higher resolution of the optical system is substantial.

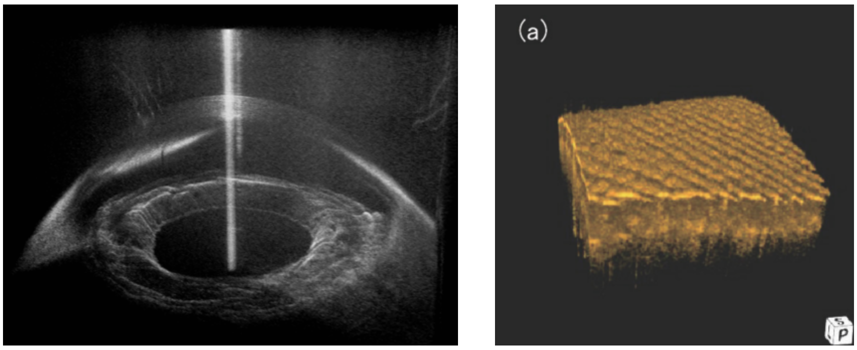


(a) Human eye (b) Human finger

Figure 1.3: Example of 3D OCT data: human eye obtained with SS-OCT [14] (left) and human finger obtained with SD-OCT [10] (right).

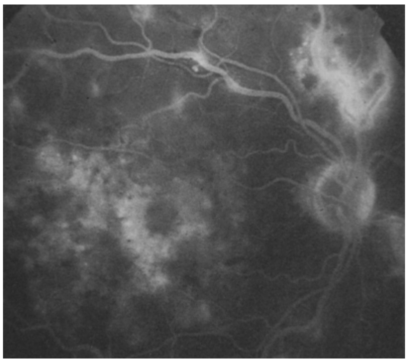

Figure 1.4: En-face view for the assessment of macular edema [32].

These applications are made possible by the small footprint of optical fibers (in the order of 200 µm of diameter) and the use of micro electro-mechanical systems (MEMS) mirrors, which can be easily embedded in endoscopes, catheters or other special probes [29, 42]. An example of a focus-adjustable probe is depicted in Figure 1.6.

Endoscopic Optical Coherence Tomography (EOCT) became an important tool for the detection of cancers affecting different parts of the human body, including bladder [46], cervix [17] and colon [22]. Other applications in the field of medicine include dermatology and skin damage assessment [21, 26] and dentistry [2, 30]. Low-delay, real-time OCT systems are also employed as a guidance tool for surgeries or tissue removal [4, 5], allowing micrometer-scale resolution and providing depth-resolved images which are unobtainable with other classical methods.

### 1.2.2 *Industrial*

OCT has also found widespread application in a variety of non-medical fields, especially where non-contact, high-precision measurements are needed. For example, real-time monitoring and thickness measure-

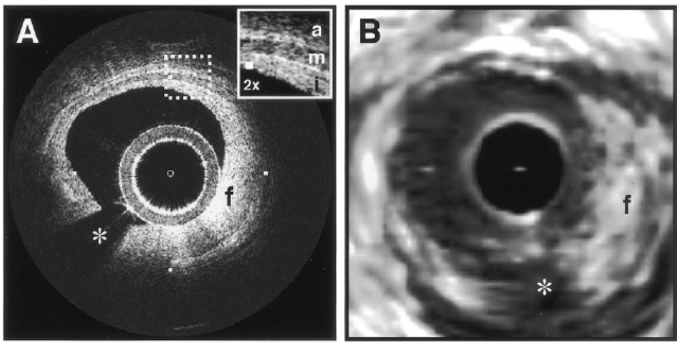


Figure 1.5: Coronary plaque imaged by OCT (left) and Intravascular Ultrasound (IVUS) (right) [24].

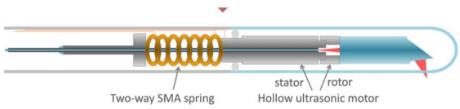


(a) Scheme.


(b) Real life model.

Figure 1.6: Probe for endoscopic OCT [29].

ment of multi-layer structures are important tools in the manufacturing of microelectronics and optical devices. Industrial uses of OCT range from defect detection in ceramic and polymeric materials [40, 43] to quality evaluation of paper products [1, 34]. An interesting usage is found in [28], where the non-invasive examination of museum paintings was demonstrated, paving the way for OCT to the field of art conservation.

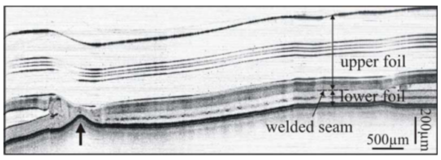


Figure 1.7: Cross-sectional OCT image of a multi-layered plastic foil used in the food packaging industry [43].

### 1.2.3 *In vivo monitoring of biological specimen*

We've seen that non-destructive measurements are essential in human medical diagnostic, but in vivo cross-sectional analysis is suited for a wide range of other biological samples. OCT has been used for growth monitoring of seeds [35], virus detection in plants [11], and even quality assessment of egg quality in the poultry industry [36]. Alternative methods such as histology, Scanning Electron Microscope (SEM) imaging, Magnetic Resonance Imaging (MRI) and X-Ray radiography are either distructive or can not guarantee the possibility of continuous monitoring with a comparable image resolution.

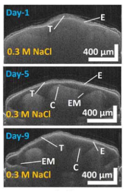

(a) Plant seeds

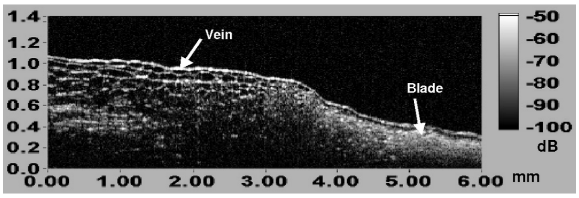


(b) Lettuce leaf

Figure 1.8: Growth monitoring of *Capsicum annuum seeds* [35] (left) and lettuce leaf [20] (right).

### 1.2.4 *Functional imaging*

Apart from the structural imaging of biological tissue, OCT can also be utilized to perform *functional* imaging, giving the user insights on the different properties of the material under analysis. PS-OCT schemes can measure properties such as birefringence, dichroism and optic axis orientation of the sample [3], while Doppler OCT (DOCT) and svOCT are able to estimate the direction and velocity of the blood flow in vessels [31]. Birefringence measurement has found use in dentistry, specifically in the monitoring of caries lesions and their progression, enabling early detection and preventing the need for surgical intervention [18].

## 1.3 OBJECTIVES

The study conducted in this thesis is based on a previous thesis [9] developed in the Photonic and Electromagnetic Group (PEG) Laboratory at the Department of Information Engineering (DEI) of the University of Padova. It consisted in the preliminary characterization of the main components of a high speed Swept-Source OCT (SS-OCT) system working in the 1300 nm range and the experimental determination of different parameters of the device, such as the source coherence length, the achievable scanning speed and the transversal resolution permitted by the focusing optics.

The primary objectives of this thesis are the following:

1. Designing and testing the optical circuitry needed for a stable SS-OCT system.

2. Developing a Data acquisition (DAQ) application capable of continuous and low-delay video stream.

3. Control and synchronization of the Galvanometric System with the optical source and the DAQ board.

4. Acquiring cross-sectional and volumetric data of different samples.

## 1.4 THESIS STRUCTURE

The structure of this document is organized in the following manner:

- Chapter 2 consists of the theoretical background on the electromagnetic phenomena of interference and spatio-temporal coherence. The basic operating principle of different OCT schemes will be thoroughly detailed.

- In Chapter 3 I will give a description of the optical and electrical devices that were used. I will also comprehensively describe the data flow of the DAQ application that was developed.

- Chapter 4 is dedicated to explaining the methods that were used in designing the system and assessing its performance. It will also showcase a series of cross-sectional images and basic volume renderings obtained from a variety of different samples.

- Chapter 5 concludes the thesis, illustrating possible future developments and further optimization of the presented work.

2

# BASIC THEORY OF OPTICAL COHERENCE TOMOGRAPY

In this chapter I will report the basic theoretical background needed to comprehend the working mechanisms behind the OCT technique, introduce the different schemes and compare them in terms of performance. The content of this chapter is partially adapted from [6, 33, 38].

## 2.1 PRINCIPLES OF COHERENCE AND INTERFERENCE

A solution to a generic electromagnetic problem is completely determined by the vector couple $\mathcal{S} = \{\mathbf{E}(\mathbf{r}, t),\ \mathbf{H}(\mathbf{r}, t)\}$, whose components represent the time-varying electric and magnetic field, respectively ($\mathbf{r}$ is the three-dimensional vector determining the position in space at which the field is evaluated). The electromagnetic field determined by $\mathcal{S}$ is considered a valid solution if it satisfies both Maxwell's Equations and the boundary conditions specific to the problem.

For monochromatic waves, i.e. fields oscillating at a single frequency $\omega$, we can use Steinmetz notation and write

$$\mathbf{E}(\mathbf{r}, t) = \Re\left[\widetilde{\mathbf{E}}(\mathbf{r})e^{j\omega t}\right] \qquad \mathbf{H}(\mathbf{r}, t) = \Re\left[\widetilde{\mathbf{H}}(\mathbf{r})e^{j\omega t}\right], \tag{2.1}$$

where $\widetilde{\mathbf{E}}$ and $\widetilde{\mathbf{H}}$ are complex 3D vectors and $\Re\left[\cdot\right]$ is the real value operator. Maxwell Equations can then be rewritten in the frequency domain. In a linear, homogeneous, isotropic, and current-free medium, Maxwell's equations can be written in the following way

$$\nabla \times \widetilde{\mathbf{E}} = -j\omega\mu\widetilde{\mathbf{H}} \tag{2.2a}$$

$$\nabla \times \widetilde{\mathbf{H}} = j\omega\varepsilon_c\widetilde{\mathbf{E}} \tag{2.2b}$$

where $\mu$ is the magnetic permeability of the medium, $\varepsilon_c = \varepsilon - \sigma/\omega$ is the complex dielectric permettivity. The simplest solution of Equation 2.2 is given by the *homogeneous plane wave*. Using a cartesian coordinate system, the electric field can be expressed as

$$\widetilde{\mathbf{E}}(\mathbf{r}) = \sum_{i=1}^{3} A_i \cdot \hat{\mathbf{x}}_i = \sum_{i=1}^{3} a_i \exp\left[jg_i(\mathbf{r})\right] \cdot \hat{\mathbf{x}}_i \tag{2.3}$$

where the amplitudes $a_i$ are constant and $g_i(\mathbf{r}) = \mathbf{k} \cdot \mathbf{r} - \delta_i$ represent the phase functions of the electric field components. The propagation vector $\mathbf{k}$ is given as a function of the wavelength $\lambda$ as follows

$$|\mathbf{k}| = \frac{2\pi}{\lambda}, \tag{2.4}$$

while the $\delta_i$'s are the phase differences which determine the state of polarization of the electromagnetic field. The magnetic field is instead obtained by applying Equation 2.2a to Equation 2.3.

The intensity of an electromagnetic field is given by the time average of the amount of energy which crosses in a unit time a unit area perpendicular to the direction of the energy flow. In the case of homogenous plane waves, it is expressed as

$$I \propto \langle \mathbf{E}^2 \rangle \tag{2.5}$$

Using Equation 2.1, we can express the electric field as

$$\mathbf{E}(\mathbf{r}, t) = \frac{1}{2}\left[\widetilde{\mathbf{E}}(\mathbf{r})e^{-j\omega t} + \widetilde{\mathbf{E}}^*(\mathbf{r})e^{j\omega t}\right], \tag{2.6}$$

so that Equation 2.5 can be written as

$$\langle \mathbf{E}^2 \rangle = \frac{1}{4}\left\langle \widetilde{\mathbf{E}}^2 e^{-2j\omega t} + \widetilde{\mathbf{E}}^{*2} e^{2j\omega t} + 2\widetilde{\mathbf{E}} \cdot \widetilde{\mathbf{E}}^* \right\rangle . \tag{2.7}$$

Averaging over a time interval sufficiently larger than the period $T = 2\pi/\omega$, we obtain

$$\langle \mathbf{E}^2 \rangle = \frac{1}{2}\widetilde{\mathbf{E}} \cdot \widetilde{\mathbf{E}}^* = \frac{1}{2}\left(a_1^2 + a_2^2 + a_3^2\right) = \text{constant}, \tag{2.8}$$

as the high frequency terms at $2\omega$ are canceled by the detector.

Suppose now that the field $\mathbf{E}$ is split in two components $\mathbf{E}_1$ and $\mathbf{E}_2$ which are then superimposed in a certain point $\mathbf{r}'$ in space, then

$$\mathbf{E}(\mathbf{r}') = \mathbf{E}_1(\mathbf{r}') + \mathbf{E}_2(\mathbf{r}'), \tag{2.9}$$

which implies that

$$\mathbf{E}^2(\mathbf{r}') = \mathbf{E}_1^2(\mathbf{r}') + \mathbf{E}_2^2(\mathbf{r}') + 2\mathbf{E}_1(\mathbf{r}') \cdot \mathbf{E}_2(\mathbf{r}') \tag{2.10}$$

The field intensity is thus

$$I = I_1 + I_2 + J_{12} = \langle \mathbf{E}_1^2 \rangle + \langle \mathbf{E}_2^2 \rangle + 2\langle \mathbf{E}_1 \cdot \mathbf{E}_2 \rangle. \tag{2.11}$$

The last term in Equation 2.11 is called *interference*. Depending on the phase difference between the two fields, the total intensity can assume different values. If the difference between the optical paths traveled by the two components is $\Delta z$, the phase difference will be $\delta = \Delta z \cdot 2\pi/\lambda$, and the interference term will be equal to

$$J_{12} = 2\langle \mathbf{E}_1 \cdot \mathbf{E}_2 \rangle = \left(a_1^2 + a_2^2 + a_3^2\right) \cos\delta. \tag{2.12}$$

In the simple case in which the two fields are linearly polarized along the $\mathbf{x}_1$ direction, we have that $a_2 = a_3 = 0$, and $I_1 = I_2 = 1/2\, a_1^2$, while the interference is given by $J_1 2 = a_1^2 \cos\delta = 2\sqrt{I_1 I_2} \cos\delta$. The total intensity is then

$$I = I_1 + I_2 + 2\sqrt{I_1 I_2} \cos\delta = 2I_1 + 2I_1 \cos\delta \in [0, 4I_1]. \tag{2.13}$$

The intensity profile is displayed in Figure 2.1. In this first approximation of perfectly monochromatic waves there are no constraint on the phase offset $\delta$ or on the optical path difference $\Delta z$ for the presence of intereference.

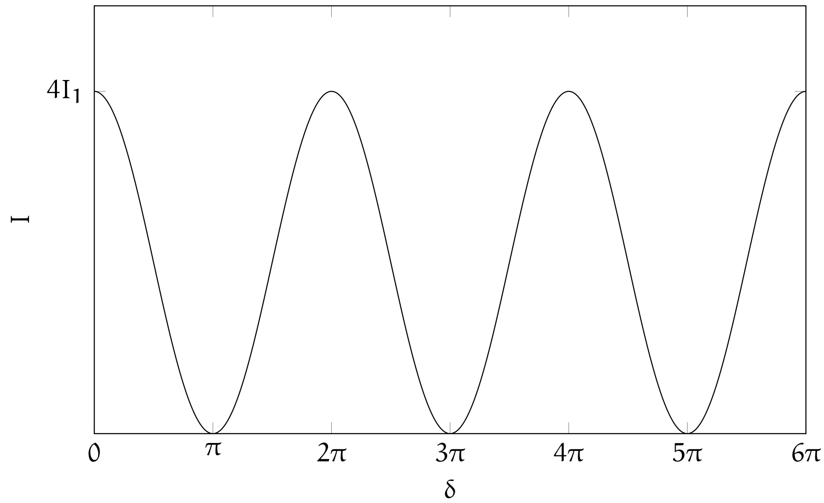


Figure 2.1: Interference fringes created by two beams of equal intensity.

### 2.1.1 *Michelson interferometer*

A classical example of the application of interference is given by the scheme called *Michelson interferometer*. In Figure 2.2 the schematic diagram of the interferometer is given. A light source emits an electric field $\mathbf{E}_0$ which is then split in two by a semitransparent mirror. The two replicas, $\mathbf{E}_1$ and $\mathbf{E}_2$, travel along the two *arms* of the interferometer, of length $l_1$ and $l_2$, are reflected by two mirrors and finally recombined. The intensity of the superposition of two fields is then measured by a photodetector. The two replicas arrive at the detector with a time difference given by

$$\tau = 2\frac{l_2 - l_1}{c}, \tag{2.14}$$

where c is the speed of light in the considered medium. From Equation 2.11 we then obtain

$$I = I_1 + I_2 + 2\langle \mathbf{E}_1(t) \cdot \mathbf{E}_2(t) \rangle = 2\left[I_1 + \langle \mathbf{E}_1(t)\mathbf{E}_1(t-\tau)\rangle\right] \tag{2.15}$$

$$= 2I_1 \left\{ 1 + \cos\left[\frac{2\pi}{\lambda} 2(l_2 - l_1)\right]\right\}. \tag{2.16}$$

This type of interferometer can be used to perform high-precision measurements of distances by making one of the arms mobile and mantaining the other fixed as a reference. Counting the number of "peaks" and "valleys" of the intensity profile as the mobile arm is translated, an estimate of path length difference is given with a precision of $\lambda/2$.

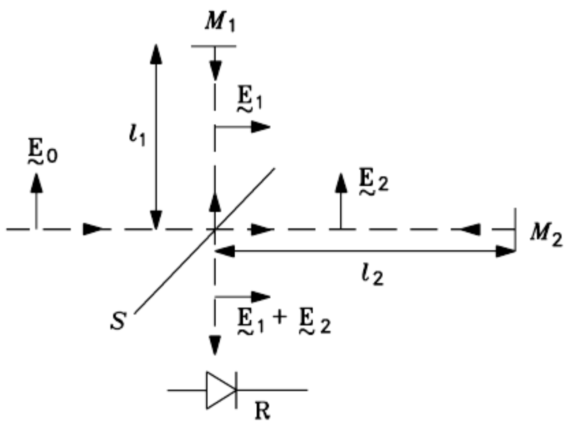


Figure 2.2: Diagram of a Michelson interferometer [38].

### 2.1.2 *Fringe visibility*

We can define a useful parameter called *fringe visibily* as follows

$$\nu = \frac{I_{max} - I_{min}}{I_{max} + I_{min}}. \tag{2.17}$$

For a perfectly monochromatic source, $\nu$ will always be constant. In particular, in the case when $I_1 = I_2$ $\nu$ is equal to 1, as $I_{min} = 0$. Real-life optical sources however will always have a bandwidth $\Delta f$ greater than 0. In these cases $\nu$ is a monotonically decreasing function of the time delay $\tau$. The *coherence time* of a source is defined as the value $\tau_c$ such that $\nu(\tau_c) = 1/e$ (Figure 2.3).

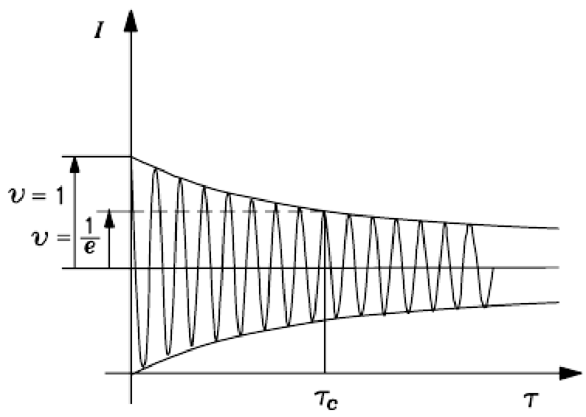


Figure 2.3: Effect of the coherence time of a source on the interference fringes at the output of a Michelson interferometer [38].

Intuitively, we may think of the coherence time as the time slot after which the optical source loses memory of what it was at the beginning. In fact, after this time slot has passed, some properties of the source randomly change due to the stochastic nature of photon emission. A perfectly coherent source emits a sinusoidal field with a well defined and constant phase relation. Similarly, two electromagnetic fields are perfectly coherent if the phase difference between the two is mantained constant for an infinite amount of time. This property is however impossible to obtain in real life, as every source has a finite coherence time. This concept is explained by the uncentainty-principle, which states that

$$\tau_c \geqslant \tau_{min} = \frac{1}{\mathcal{B}}, \tag{2.18}$$

where $\mathcal{B}$ is the bandwidth of the source. This equation results in the fact that there are no sources which are completely incoherent in time, as they would require an infinite bandwidth.

### 2.1.3 *The coherence function*

Another way to describe the coherence property of light other than the fringe visibility parameter, is through the so-called *mutual coherence function*. It is defined for polychromatic, i.e., non-monochromatic fields as follows [6]:

$$\Gamma_{12}(\tau) = \langle \mathbf{E}_1(t+\tau)\mathbf{E}_2^*(t) \rangle \,, \tag{2.19}$$

If $\mathbf{E}_1 = \mathbf{E}_2$, it is called *self-coherence function*, and it's written as $\Gamma_{11}(\tau)$. Notice that when $\tau = 0$ it reduces to the field intensity:

$$\Gamma_{ii}(0) = I_i \,. \tag{2.20}$$

It is then useful to apply the following normalization

$$\gamma_{ij}(\tau) = \frac{\Gamma_{ij}(\tau)}{\sqrt{\Gamma_{ii}(0)}\sqrt{\Gamma_{jj}(0)}}, \tag{2.21}$$

so that it assumes values in the $[0, 1]$ interval. This normalized function is called *complex degree of coherence*, and it allows the following definitions:

1. Completely incoherent fields: $|\gamma_{ij}| = 0$, no interference fringes are visible.

2. Completely coherent fields: $|\gamma_{ij}| = 1$, the total intensity includes the interference term.

3. Partially coherent fields: $0 < |\gamma_{ij}| < 1$, interference fringes are present, and assume a visibility parameter equal to

$$\nu = \frac{2\sqrt{I_i I_j}}{I_i + I_j}|\gamma_{ij}|. \tag{2.22}$$

   When the two fields have equal intensity, than the two parameters coincide.

Using this notation, the equation for the intensity of two partially-coherent beams is then

$$I = I_1 + I_2 + 2\sqrt{I_1 I_2}|\gamma_{12}(\tau)|\cos(\delta) \tag{2.23}$$

where we can clearly see the effect of coherence on the shaping of the interference fringes. Using the coherence function instead of the fringe visibility as a measure of coherence, the coherence time of a source, $\tau_c$, is defined as the full-width half-maximum (FWHM) parameter of its self-coherence function, that is, the value of $\tau$ such that

$$|\gamma(\tau)| = \frac{|\gamma(0)|}{2}. \tag{2.24}$$

The shape of the coherence function of an optical source is completely determined by its spectrum $I(k)$ through the Wiener-Khintchine theorem, which states that the autocorrelation function and the power spectral density (PSD) of a random process are connected through their Fourier Transform.

### 2.1.4 *Coherence length*

Starting from the coherence time of the source, $\tau_c$, we can also define its coherence length as follows

$$l_c = c_0 \tau_c, \tag{2.25}$$

where $c_0 \simeq 3 \cdot 10^8$ m/s is the speed of light in vacuum. Using a light source with a coherence length $l_c$ in the Michelson interferometer previously presented, we would observe an interference pattern at the photoreceiver only if the difference in length of the two arms is such that

$$\Delta l = |l_2 - l_1| \leqslant l_c/2, \tag{2.26}$$

or, equivalently, if the total Optical Path Difference (OPD) is matched to within the coherence length of the source.

While we just defined the coherence *length* of a source, it's important to note that it is a parameter that is directly related to the time coherence and does not describe the phenomenon of spatial coherence.

## 2.2 OCT TERMINOLOGY

Before introducing the different OCT techniques it is useful to introduce some terminology that will be used throughout this thesis. The most basic OCT measure is called A-scan (Axial-scan), which is a signal that represents the reflectivity of a sample as a function of depth.

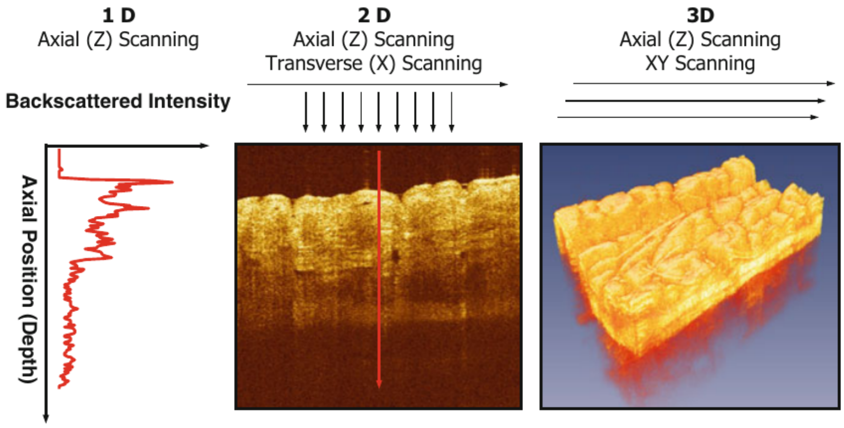


Figure 2.4: Diffent types of OCT measurements. [15]

The amount of information carried by these measurements is limited, but can be used to perform thickness measurements if the structure of the sample is known a priori.

If multiple consecutive A-scans are acquired along a transverse direction on the sample, a cross-sectional image, called B-scan, is generated. They are the most direct way to determine the anatomy of an unknown sample and are often sufficient for diagnostic purposes, especially in Ophtalmology. Their visualization does not require advanced techniques, but if a real-time high-resolution video stream is desired then careful design choices have to be made.

Finally, 3D volumetric data can be generated by acquiring consecutive B-scans along a second direction on the transverse plane. Intuitively, they are called C-scans. Contrary to B-scans, volume rendering requires sophisticated and efficient algorithms for a correct data interpretation and visualization [8, 16, 27]. Starting from 3D data its also possible to obtain frontal projections of the sample, called *en-face* views (Figure 2.5), or to generate cross-sections along an arbitrary plane.

## 2.3 TIME DOMAIN OCT

Time-Domain OCT (TD-OCT) was the first OCT technique that was demonstrated in the literature [23]. The basic setup is that of a Michelson Interferometer in which one of the two mirrors is translatable and the other is replaced by the sample that we wish to analyze. The two arms are called respectively *Reference arm* and *Sample arm*. As explained in Section 2.1.1, the two beams arriving at the photodetector generate interference fringes if the OPD is less than the coherence length $l_c$ of the source. A diagram of this setup is available in Figure 2.6.

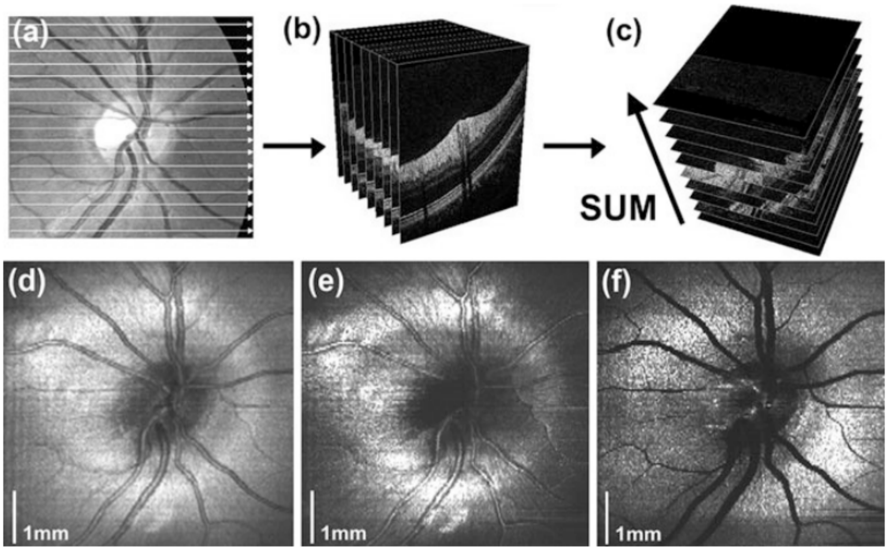


Figure 2.5: [15]

The light beam reflected by the reference mirror while in position $z_1$ will interfere with all the reflections occurring in the sample at depths $z \in [z_1 - l_c/2, z_1 + l_c/2]$. By measuring the intensity of the fringes it is then possible to obtain an estimate of the sample reflectivity at those depths. The whole axial measurement of the sample can be acquired by moving the translatable mirror along an adequate interval of positions. Since a single mirror position is mapped to an interval of length $l_c$ of axial positions in the sample, the coherence length of the source can be considered to be the axial resolution of the system. As a consequence short coherence lenghts are preferred, meaning that broadband sources are more widely employed.

If the light source was perfectly monochromatic, the reference signal would interfere with an infinite number of reflected replicas generated at every depth in the sample, as there would be no constraint on the OPD.

To better understand this concept, suppose that the sample is an ideal reflector with a reflection coefficient $\rho_s$ is positioned in such a way that the OPD is 0. The intensity measured by the detector when a OPD equal to $\Delta z$ is introduced is then

$$I(\Delta z) \propto |\rho_s|^2|E_i|^2 + |\rho_r|^2|E_i|^2 + |\rho_s\rho_r|^2|E_i|^2|\gamma(\Delta z)|\cos\left(\frac{2\pi}{\lambda_0}\Delta z\right) \tag{2.27}$$

Apart from the DC offset given by the intensity of the two signals there is an oscillating term with period equal to $\lambda_0$, which is the central wavelength of the source. Figure 2.7 illustrates the oscillating term and its envelope, which is dictated by the coherence function $\gamma$ and the sample reflectivity $\rho_s$ (set equal to 1). With a perfectly

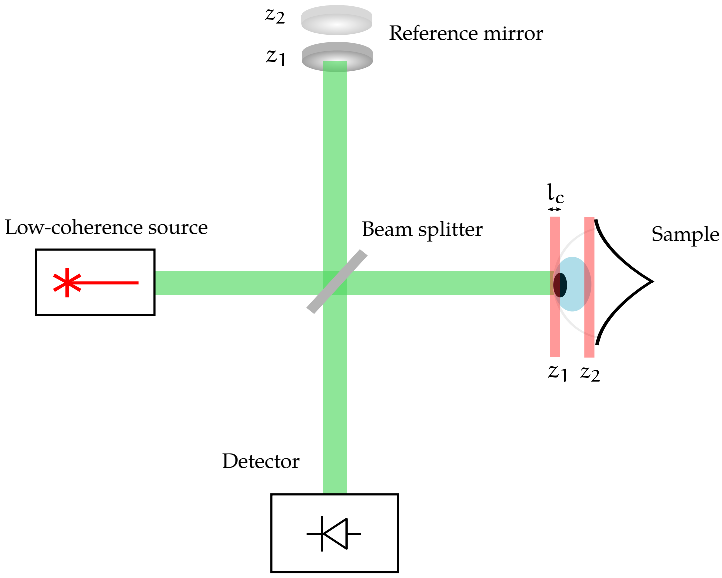


Figure 2.6: Diagram of the basic TD-OCT setup using a Michelson interferometer.

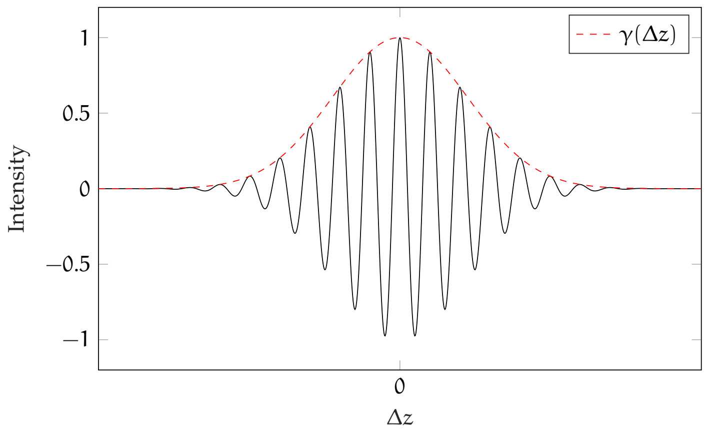


Figure 2.7: Diagram of the basic TD-OCT setup using a Michelson interferometer used in [23].

coherent source $\gamma$ would be equal to 1 for all values of $\Delta z$ and we would not be able to identify the reflector. On the other hand, with an increasingly sharper $\gamma$, the ideal reflector would be more and more defined.

Since the difference between the arm lengths is $\Delta l = \Delta z/2$, when scanning the reference arm, interference fringes will be generated as a function of time with periodicity equal to $(\lambda/2)/\sigma$ where $\sigma$ is the scanning speed.

A setup similar to Figure 2.6 can be created using fiber optics components and lenses to focus the optical beam on the sample and collect the reflections, as in Figure 2.8 [23]. The role of splitting and recombining the signals is assigned to a fiber coupler, while a piezoelectric transducer (PZT) is used to frequency-modulate the interference sig-

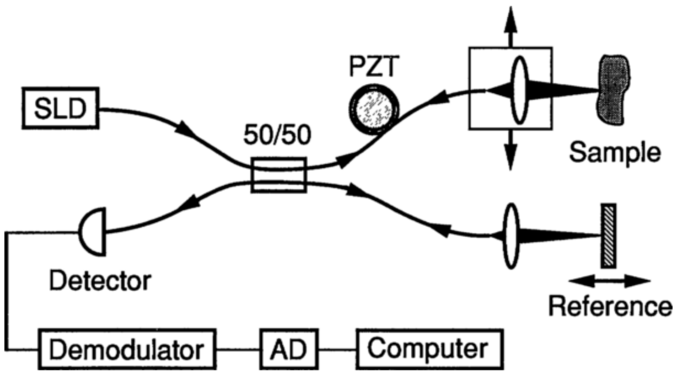


Figure 2.8: Diagram of the basic TD-OCT setup using a Michelson interferometer used in [23].

nal and shift it inside the photodetector's bandwidth. The generated electrical signal is then filtered, demodulated and acquired by an Analog-to-Digital Converter (ADC).

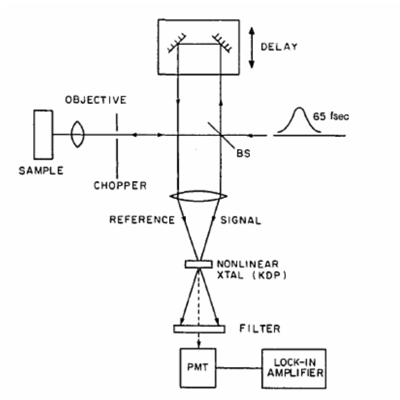


(a) Optical ranging setup

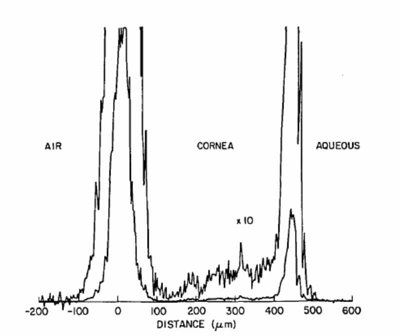


(b) Lettuce leaf

Figure 2.9: Optical ranging setup (left) and measurement (right) of the cornea of the rabbit eye [19].

This imaging technique is also called *Optical Ranging*, and was demonstrated by Fujimoto et al.[19] in 1986. An A-scan of the cornea of a rabbit's eye was performed *in vivo*, and is available in Figure 2.9b. The peaks in signal intensity located at $l = 0$ and $l \sim 450$ µm are due to the strong reflection occurring at the interface between two different media. Inbetween these two peaks it's also possible to notice the effect of light scattered by the cornea, which is not present in the air and aqueous regions.

To acquire B-scans and C-scans, axial measurements can be repeatedly performed while moving the sample on the orthogonal plane or by deflecting the impinging optical beam by means of galvanometric mirrors.

The main disadvantage of this scheme is the slow acquisition rate, as it requires the mechanical movement of the reference arm. Consequently, *in vivo* imaging is difficult to achieve since the movement of the sample could introduce heavy distortions on both B-scans and C-scans.

## 2.4 FOURIER DOMAIN OCT

Fourier-Domain OCT (FD-OCT) is a group of OCT techniques that encode the depth information of a sample in the frequency content of the interference signal and decode it through a Fourier trasform operation. As opposed to TD-OCT, an axial scan is obtained without the need of a scanning mirror in the reference arm. This results in a much faster acquisition speed and higher quality measurements, since the distortions caused by the mechanical vibrations and uncertainty on the position of the mirror are removed. On the other hand, FD-OCT systems require more advanced laser sources and detection schemes, other than some numerical compensation and high speed ADCs.

The two main FD-OCT schemes are called Spectral-Domain OCT (SD-OCT) and Swept-Source OCT (SS-OCT), and will be presented in the next sections.

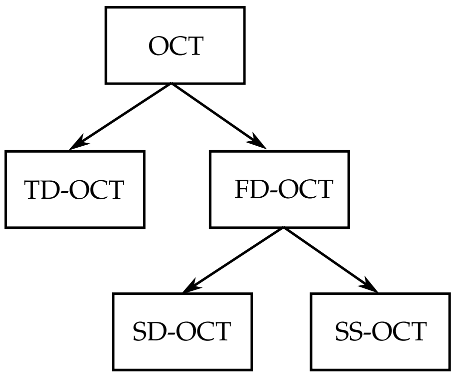


Figure 2.10: Diagram illustrating the different types of OCT modalities.

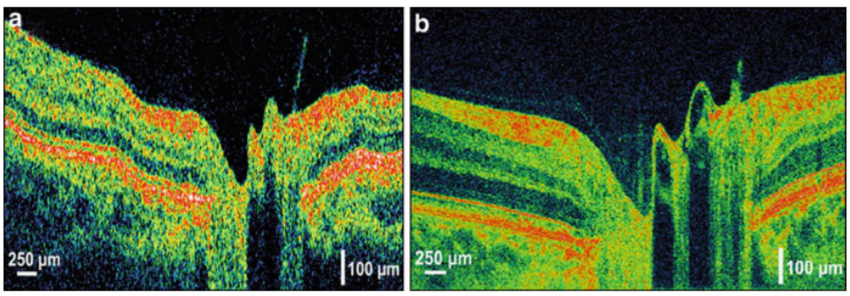


Figure 2.11: Comparison between images of the human retina obtained with standard TD-OCT (left) and high-speed, high-resolution FD-OCT (right).

### 2.4.1 *Spectral Domain OCT*

SD-OCT was the first type of FD-OCT to be implemented, and was proposed by Wojtkowski et al. in 2002 [45]. This technique uses a Superluminescent Diode (SLD) as a broadband optical source, a Michelson interferometer similar to that in Figure 2.6 and a detector consisting of a spectrometer. A diagram of the setup is available in Figure 2.12. As already mentioned in Section 2.4, SD-OCT can acquire an A-scan with a single optical pulse, without the need to select the imaging depth through a scanning reference mirror. This comes at the price of a more complex detection scheme and the need for computationally intensive post-processing solutions. In order to achieve real-time performances, SD-OCT scheme typically require the use of fast GPUs.

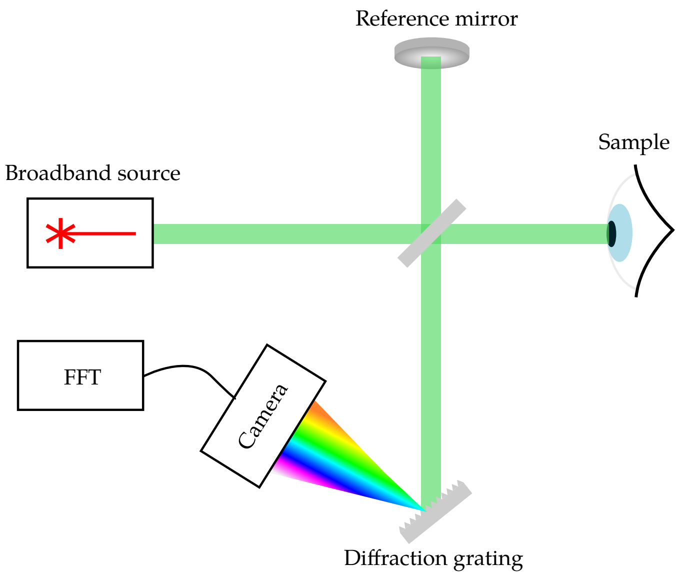


Figure 2.12

To gain insight on the working principle of SD-OCT, we can rewrite Equation 2.27 as a function of the wavenumber $k = 2\pi/\lambda$ and fixing the OPD:

$$I(k) \propto I_{source}(k) \cos(k\Delta z) \tag{2.28}$$

This means that a reflector placed at a depth $d = \Delta z/2$ will frequency modulate the source spectrum with a frequency that is linearly dependant on d. This effect is illustrated in Figure 2.13 for a broadband source centered at 1310 nanometers, with ideal reflectors positioned at $d_1 = \Delta z/2 = 12.5$ µm and $d_2 = \Delta z/2 = 25$ µm.

Using a diffraction grating or a prism, the spectrum of the interference signal is spatially separated and acquired through a linear photodetector, typically a charged coupled device (CCD) or complementary metal-oxide semiconductor (CMOS) camera. The corresponding A-scan

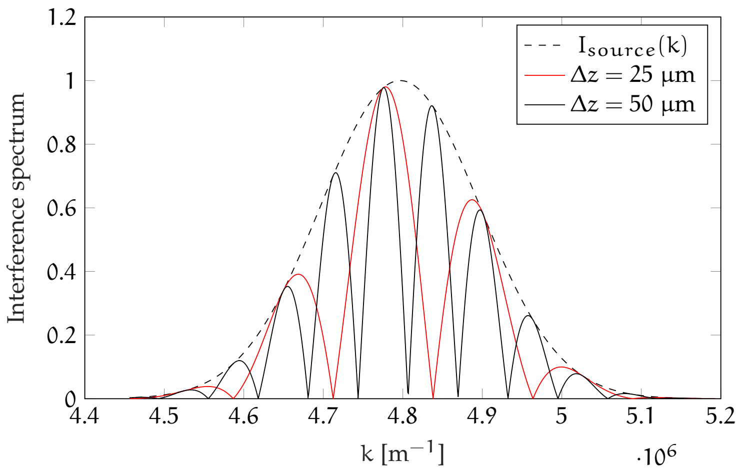


Figure 2.13

is then computed using an inverse Fourier Transform operation, mapping modulation frequency in axial position. The depth of the various layers of the sample are encoded in the modulation frequency of the spectrum, while their reflectivity is encoded in the fringe visibility.

A key observation has to be made regarding the role of the coherence function $\gamma$. In fact, the spectrum modulation induced by a reflection at depth $d = \Delta z/2$ can only be detected if $\gamma(d/2)$ is non-zero, that is, only the portion of the sample that is within the coherence length of the source can be imaged. This is the main disadvantage compared to TD-OCT schemes, in which the depth of focus in the sample was selected with the mechanical movement of the reference mirror.

#### 2.4.1.1 *Drawbacks*

SAMPLING DISTORTION One of the major problems corcerning this detection technique is that the interference spectrum is usually detected linearly in the wavelength. For example, a diffraction grating spatially separates the different wavelengths at an angle $\beta_m$ with respect to the axis normal to the grating such that

$$\sin\beta_m = m\frac{\lambda}{\Lambda} + \sin\alpha, \tag{2.29}$$

where $\Lambda$ is the spacing between each line of the grating, $\alpha$ is the angle of the inpinging wave and $m$ is the order of diffraction. This behaviour requires a re-sampling of the acquired spectrum before computing the Fourier Transform in order to obtain a signal which is linearly spaced in frequency instead of wavelength. If this post-processing step is ignored, an oscillating term with a fixed frequency $\propto \Delta z$ in the interference spectrum will result in a broadened peak in the Fourier domain, as can be observed in Figure 2.14. The linear sampling in the $\lambda$ domain will induce a chirp on the spectrum (red).

Such behaviour has a detrimental effect on the axial resolution of the system.

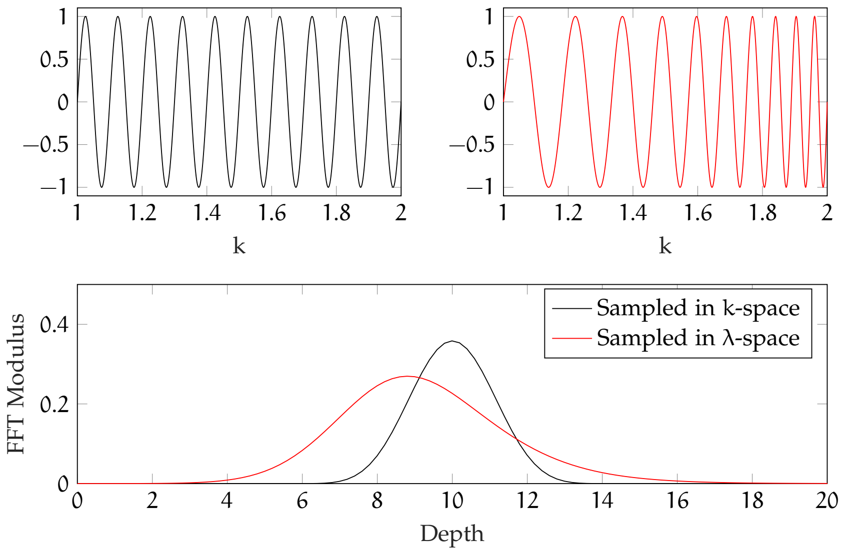


Figure 2.14: Interference distortion induced by linear sampling in the $\lambda$ space.

SENSITITY FALLOFF A second harmful effect on the performance of these types of FD-OCT devices is the so-called *Sensitivity falloff*. Sensitivity is defined as the signal-to-noise ratio (SNR) when the sample is an ideal reflector. It's been experimentally demostrated that for increasing imaging depths, the sensitivity value drops. Such effect is illustrated in Figure 2.15. This behaviour is due to the fact that when increasing the OPD between reference and sample arm, the coherence function $\gamma(\Delta z)$ decreases as the two reflected signals only partially overlap, resulting in a lower signal intensity.

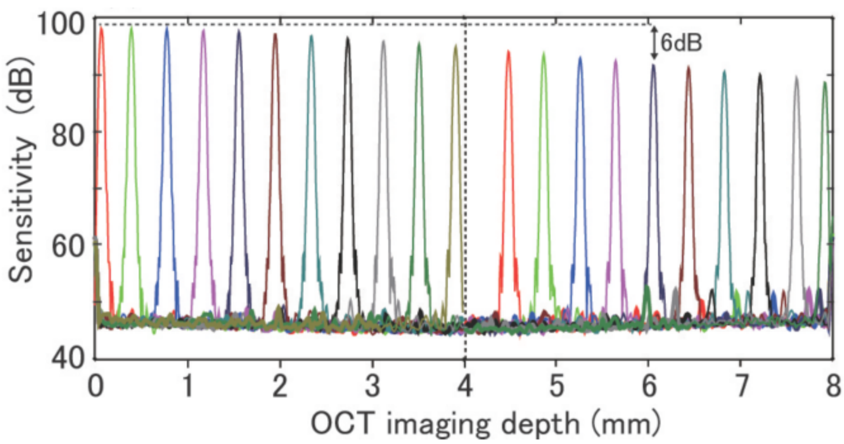


Figure 2.15: Sensitivity falloff in FD-OCT systems [10].

An additional factor that contributes to this detrimental effect is the resolution of the photodetector arrays used to acquire the interference signal. As previously explained, higher imaging depths correspond to higher spectrum modulation frequencies. If the number of pixel N of, e.g., a CCD camera is not sufficiently high, the higher frequency components will be undersampled, reducing the range of visibility. Beam diameter and camera's pixel size also influence the loss of sensitivity.

IMAGING ARTIFACTS The massive gain in acquisition rate that comes from detecting the whole imaging range in a single shot is offset by the introduction of different artifacts in the reconstructed A-scans. The interference pattern acquired by the photodetectors array is comprised of three terms:

1. *DC component*. All the reflected replicas of the impinging signal coming from the sample contribute to a constant DC offset in the interference signal. These are equivalent to the non-interfering terms in the Michelson interferometer formula. When Fourier-transformed, they will appear as a reflector positioned at the very start of the imaging range, where the OPD is close to zero. A simple solution to this problem is to compute and subtract the average value of the spectrum before applying the Fourier Transform.

2. *Cross-Correlation terms*. These are the interference terms that arise from the correlation between the reference signal and the reflections coming from the sample arm. As previously discussed, they contain the information required to reconstruct the reflectivity profile of the sample.

3. *Auto-Correlation terms*. They result from the interference between reflectors in the sample that are less than a coherence length apart.

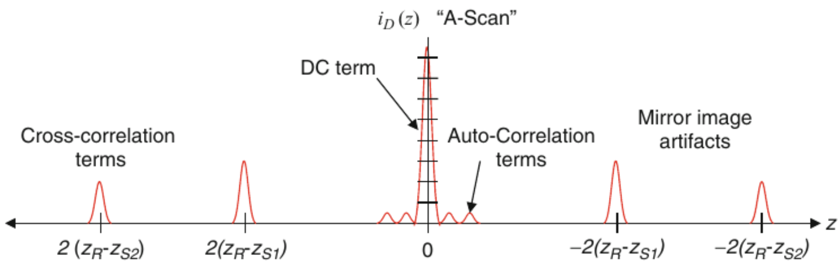


Figure 2.16: [15]

These components are visible in Figure 2.16, who depicts the Fourier Transform of the interference signal generated by two reflectors. A further issue that is highlighted by this plot is the presence of the so called *complex conjugate artifacts*, or mirror image artifacts. This phenomenon arises from the Fourier Transformation of a real signal, which will have the property of Hermitian simmetry (even modulus and odd phase). This means that FD-OCT techniques cannot differentiate between positive and negative frequencies, or equivalently, between a sample placed before or after the zero OPD position.

The easiest way to deal with this problem is to simply drop one half of the acquired A-scan, effectively halving the maximum imaging depth of the system. Mirror artifacts will still appear in the image if the sample is too close to the scanning lens and crosses the zero OPD position, which is fixed by the reference mirror. The part of the sample which is in the "negative" OPD range will appear flipped and superimposed to the other part of the sample. This effect is illustrated in Figure 2.17, in which the scanning lens is progressively moved forward, closer to the patient's retina.

Different methods to solve this issue and restore the full imaging range have been proposed, including complex-signal detection schemes using 3x3 fiber couplers [37], heterodyne detection [13] and phase-shifting techniques [41] using either PZTs or electro-optic modulators (EOMs).

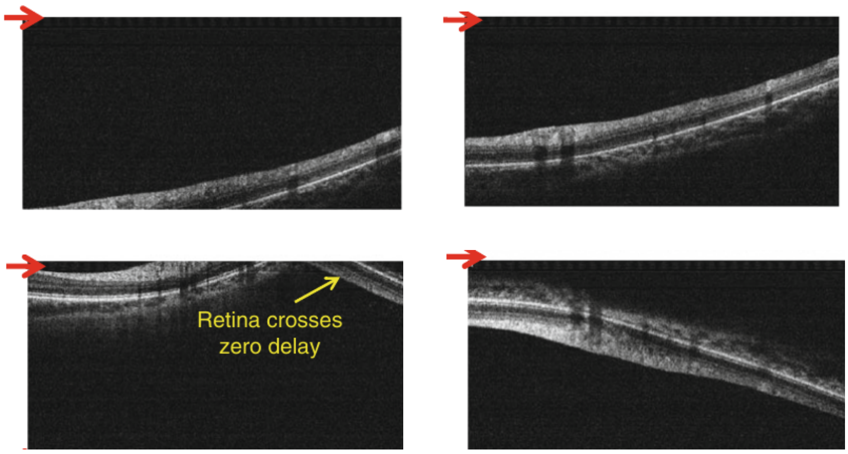


Figure 2.17: Complex conjugate artifacts in SD-OCT.

### 2.4.2 *Swept-Source OCT*

Swept-Source OCT (SS-OCT), also known as optical frequency domain interferometry (OFDI), is a FD-OCT technique that employs a narrow-bandwidth frequency-swept laser as an optical source. The introduction of tunable sources simplifies the detection scheme, removing the need for diffraction gratings and photodetector arrays. Ideally, a swept-source laser for SS-OCT should present a frequency sweep that is linear, i.e, the istantaneous optical frequency should be expressed as

$$f(t) = f_0 + \delta f \cdot t, \tag{2.30}$$

where $\delta f$, typically measured in Terahertz per microsecond, is the sweep rate of the source. If this requirement is satisfied, the intensity at the ouput of the interferometer when the sample is a sigle reflector positioned at the depth $d = \Delta z/2$, can be expressed as

$$I(t) = I_1 + I_2 + 2\sqrt{I_1 I_2}\cos(2\pi\Delta f t) \tag{2.31}$$

where

$$\Delta f = \delta f \cdot \Delta t = \delta f \cdot \frac{\Delta z}{c} = \delta f \cdot \frac{d}{2c}, \tag{2.32}$$

called the *beat frequency*, is linearly dependant on the depth of the reflector. When the reflector is replaced by a real sample, multiple beat frequencies arise in the photodetector's current and the reflectivity profile can be reconstructed with a Fourier Transform. This technique is equivalent to SD-OCT, with the key difference that the frequency sweep enables the detection as a function of time through a simple photodetector, while the diffraction grating spatially separates the different wavelengths and directs them to a detector array.

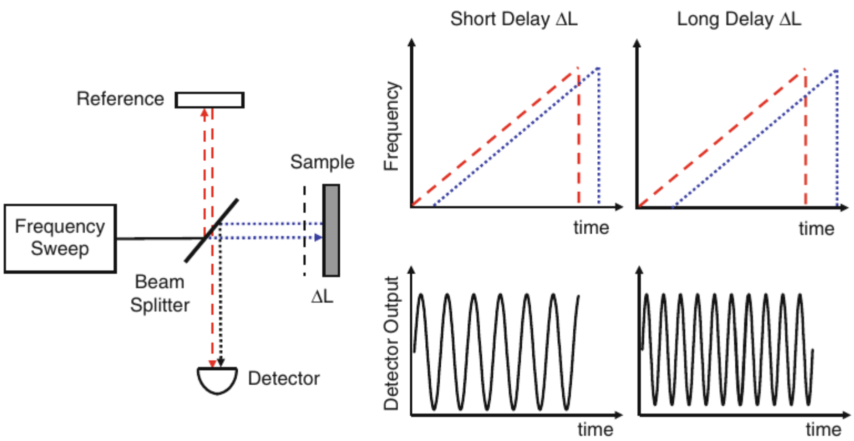


Figure 2.18: [15]

#### 2.4.2.1 *Sweep nonlinearity*

A tunable laser generally consists of a gain medium, typically a semiconductor optical amplifier (SOA), a tunable wavelength filter and a laser cavity that supports a large bandwidth. The frequency-sweep is achieved by controlling the tunable filter through electrical signals to select the desired wavelength. Figure 2.19 shows the diagram of a Axsun swept source in which frequency tuning is achieved by tilting a MEMS mirror at the end of a Fabry-Perot filter. Rapidly changing the selected wavelength can affect the linearity frequency sweep, contributing to a nonlinear term in Equation 2.30, which then becomes

$$f(t) = f_0 + \delta f \cdot t + \eta(t), \tag{2.33}$$

where $\eta(t)$ contains the aforementioned nonlinearities. If the detector's output is digitized with a uniform clock rate, a similar effect to that described for SD-OCT systems can arise (Figure 2.14), resulting in a non-linear sampling in the k-space. Consequently, distortions in the acquired A-scans can appear, hindering the image quality. A resampling of the acquired signal is then required in order to linearize the frequency sweep, adding to the total computational cost and possibly reducing the acquisition rate of the system.

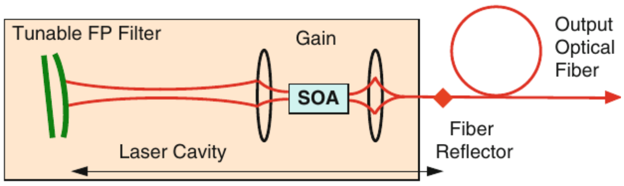


Figure 2.19: Frequency-swept optical source by Axsun [15].

### 2.4.2.2 *k-clocking*

While in SD-OCT the resampling step is the only possible solution for this issue, SS-OCT enables a hardware approach through a non-uniform clocking of the DAQ device. This is accomplished by extracting a clock signal, called *k-clock*, by means of an unbalanced Mach-Zender interferometer (MZI) which detects the frequency-sweep and generates a sinusoidal signal with a variable frequency. This approach removes the need for the computationally-intensive resampling step, but requires special DAQ devices that can handle external clocks with a wide range of frequencies and duty cycles, which are generally more expensive.

### 2.4.2.3 *Acquisition rate*

The acquisition speed of SS-OCT systems is dictated by the source sweep repetition rate, that is, the frequency at which the source is able to sweep the entire bandwidth. This parameter is determined by the laser cavity length. In fact, for a given frequency, the spontaneous emission has to build up in order to reach a saturation limit to be correctly amplified by the active region. Shorter cavities with a smaller round-trip generally guarantee higher repetition rates than longer cavities. Novel swept-source designs enable acquisition speeds in the order of 100,000 A-scans per second, with Fourier domain mode locking (FDML) and vertical cavity surface-emitting lasers (VCSELs) reaching repetition rates above 500 kHz. These high rates make SS-OCT the primary candidate for real-time 3D visualization of *in vivo* samples, where motion artifacts could hinder image quality. This is possible because the detection schemes is no longer the bottleneck like in SD-OCT, where the slow camera response times limited the overall rate of the system.

#### 2.4.2.4 *Axial resolution*

Just like in the case of SD-OCT, the axial resolution depends on the tuning range of the source, $\Delta\lambda$. The tuning range is defined as the FWHM of the spectrum. In the case of a Gaussian spectrum, the axial resolution, defined as the FWHM of the reflection peak generated by a perfect reflector, is given by

$$\delta z \simeq 0.75 \cdot \frac{\lambda_0^2}{\Delta\lambda}, \tag{2.34}$$

where $\lambda_0$ is the central wavelength of operation, which is chosen based on the application (1060 nm for Ophtalmology, 1300 nm for tissue imaging).

#### 2.4.2.5 *Imaging range*

Imaging range of SS-OCT systems is, like other FD-OCT schemes, limited by the coherence length of the source, which we have previously defined as the OPD at which the visibility of the interference fringes drops to 0.5. This parameter is controlled by the istantaneous linewidth of the source $\delta\lambda$ by the following equation:

$$l_c \approx 0.44 \frac{\lambda_0^2}{\delta\lambda}. \tag{2.35}$$

As with SD-OCT, complex conjugate artifacts typically limit the imaging range to be half of the coherence length.

When using a k-clock to acquire A-scans, the imaging range is also dependant on the path difference of the MZI's arms, which has to be 4 times the maximum imaging depth, $d_{max}$. A factor of 2 is needed because a reflector positioned at $d_{max}$ will have OPD equal to $\Delta z = 2d_{max}$ with respect to the reference mirror. The other factor of 2 is needed to satisfy Nyquist's criterion, so that the k-clock will have a maximum frequency that is 2 times the beat frequency generated by the reflector at $d_{max}$.

#### 2.4.2.6 *Balanced detection*

The use of simple photodetectors instead of more complex setups involving diffraction gratings and prisms allows for a dual balanced detection scheme. By collecting the reference and sample signals through a circulator and feeding them to a 3 dB fiber coupler, two interference signals can be obtained. A balanced detector can then subtract the common DC component and the excess noise while adding the interference term. This detection scheme has been proved to be more efficient than a simple Michelson interferometer. A complete SS-OCT scheme with dual balanced detection and external k-clock is illustrated in Figure 2.20.

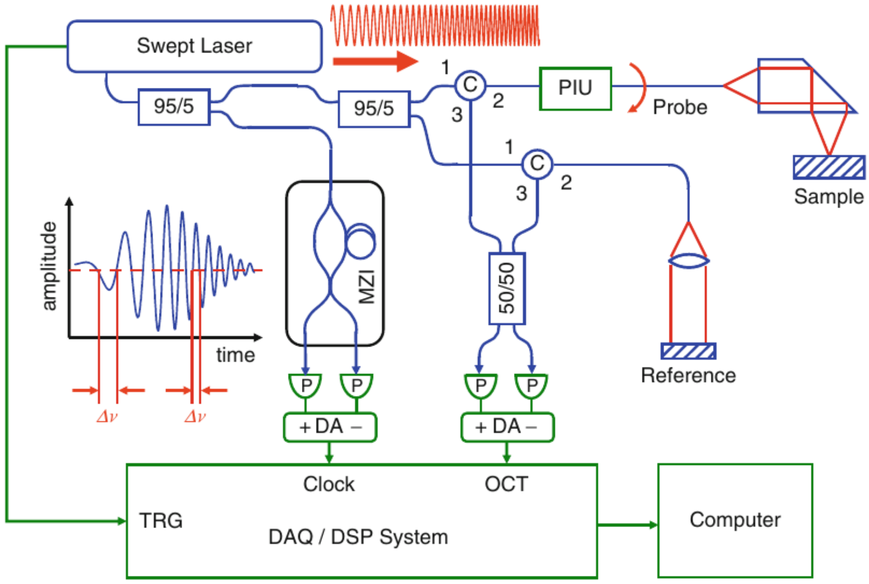


Figure 2.20: Frequency-swept optical source by Axsun [15].

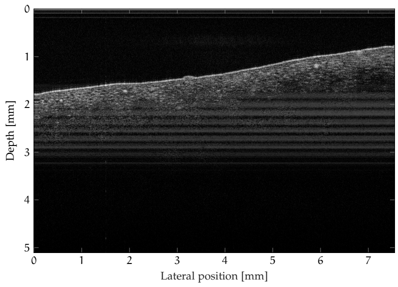


(a) Asia personas duo.

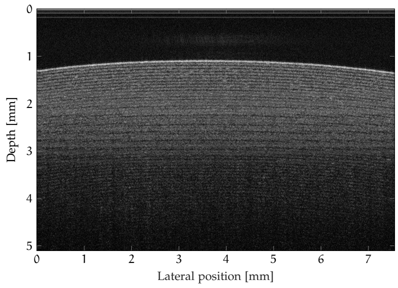


(b) Pan ma signo.

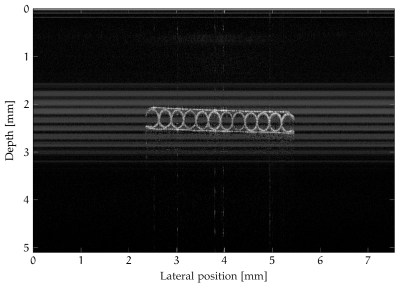


(c) Methodicamente o uno.

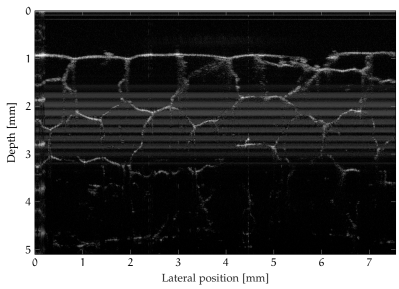


(d) Titulo debitas.

Figure 2.21: Tu duo titulo debitas latente.

# 3

# DESCRIPTION OF THE SETUP

This chapter details the setup that was used in the design of a Swept Source OCT system developed for this thesis work, describing the optical and electrical components that were employed.
Particular care will be given to the characterization of the DAQ board and the design of the acquisition software.

## 3.1 OPTICAL SOURCE

As already discussed in Chapter 2, SS-OCT systems employ a narrow-bandwidth tunable laser to enable a simple detection scheme and is one of the most critical components of the entire system. The source that was used in this thesis is a SSOCT-1310 by Axsun Technologies, which is a class 3 laser that uses a MEMS tunable filter to sweep wavelengths in the 1300 nm range.

The two most important features of this laser are the fast sweep rate, which enables high speed imaging, and the presence of the k-clock signal used for equalizing the nonlinear frequency sweep.


Figure 3.1: The acquisition board, AlazarTech ATS9350.

An photo of the laser is available in Figure 3.1. The emitted light is collected by connecting a fiber optic patch cord to the FC/APC connector on the front panel, which also includes two SMA connectors for the sweep-start trigger and the k-clock signal.

| PARAMETER | UNITS | VALUE |
|---|---|---|
| Sweep Rate | kHz | 100.2 |
| Center Wavelength | nm | 1305 |
| Wavelength Tuning Range | nm | 140.38 |
| Average Power | mW | 25.7 |
| Duty Cycle | % | 77.3 |
| Sampled Duty Cycle | % | 50.5 |
| External Clock Min Frequency | MHz | 183.1 |
| External Clock Average Frequency | MHz | 307.0 |
| External Clock Max Frequency | MHz | 332.1 |
| Sampling Clocks | – | 1536 |

Table 3.1: Axsun laser datasheet.

### 3.1.1 *Optical Spectrum*

A critical parameter in swept sources for OCT applications is the wavelength interval over which the laser is able to tune. From Table 3.1, we can see that the Axsun SSOCT-1310 is centered at $\lambda_0 = 1305$ nm with a bandwidth of $\Delta\lambda = 140.38$ nm. These values were verified by connecting the laser output directly to an Optical Spectrum Analyzer (OSA), measuring its spectrum.

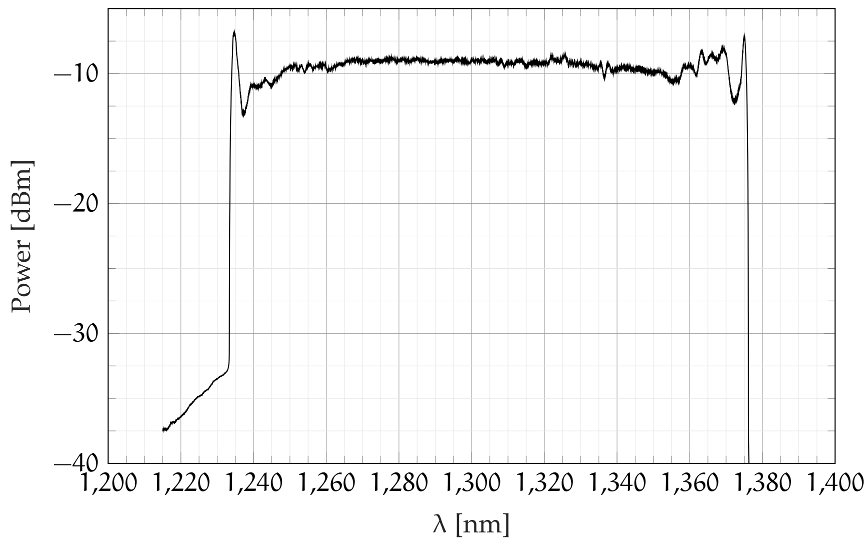


Figure 3.2: Spectrum of the Axsun SSOCT-1310 laser, obtained with a 1 nm resolution.

The measurement was executed with a resolution of 1 nanometer, resulting in the spectrum visible in Figure 3.2. The edge wavelengths turned out to be $\lambda_1 \approx 1237$ nm and $\lambda_2 \approx 1376$ nm, which result in a bandwith of $\Delta\lambda \approx 139$ nm and central wavelength of $\lambda_0 \approx 1307$ nm. These values slightly differ from those reported in the datasheet, but not enough to compromise the performance of the laser.

The bandwidth is swept at a frequency $f_a = 100.2$ kHz and with a duty cycle $d_c = 0.505$, meaning that the average sweep speed is

$$\sigma_\lambda = \frac{\Delta\lambda f_c}{d_c} \approx 27.8 \text{ nm}/\mu\text{s}. \tag{3.1}$$

Since the goal of SS-OCT sources is to perform a linear frequency sweep, it is more useful to define this parameter in the following manner

$$\sigma_f = c_0 \left( \frac{1}{\lambda_0 - \Delta\lambda/2} - \frac{1}{\lambda_0 + \Delta\lambda/2} \right) \frac{f_a}{d_c} \approx 4.9 \text{ THz}/\mu\text{s} \tag{3.2}$$

The istantaneous frequency, after linearization, is thus expressed by

$$f(t) = f_0 + \sigma_f t \tag{3.3}$$

where the starting frequency is determined by

$$f_0 = \frac{c_0}{\lambda_0 + \Delta\lambda/2} \approx 218.2 \text{ THz}. \tag{3.4}$$

### 3.1.2 *Axial Resolution*

Using Equation 2.34 and the data provided by Table 3.1 it is possible to obtain an estimate of the axial resolution provided by the employed optical source. The axial resolution is found to be

$$\delta z \simeq 0.75 \frac{\lambda_0^2}{\Delta\lambda} \approx 9.2 \ \mu\text{m}. \tag{3.5}$$

This approximation is valid for sources with a Gaussian spectrum, and can lead to an overestimation of the real axial resolution of the system in case this condition is not met.

### 3.1.3 *Sweep trigger*

The Axsun laser provides a square-wave signal that determines the start of the frequency sweep and that is used to trigger the acquisition of A-scans. This signal is acquired with a high-speed oscilloscope and illustrated in Figure 3.3. The voltage range was measured as $V_{range} \approx [0, 1.48]$ V, while the duty cycle is found to be

$$d_c = \frac{t_{high}}{t_{high} + t_{low}} \approx 0.97\,. \tag{3.6}$$

For a correct acquisition of A-scans, the datasheet recommends to trigger the acquisition device when the signal level reaches the value of $V_{trig} = 0.71$ V, pictured in Figure 3.3 with a red line.

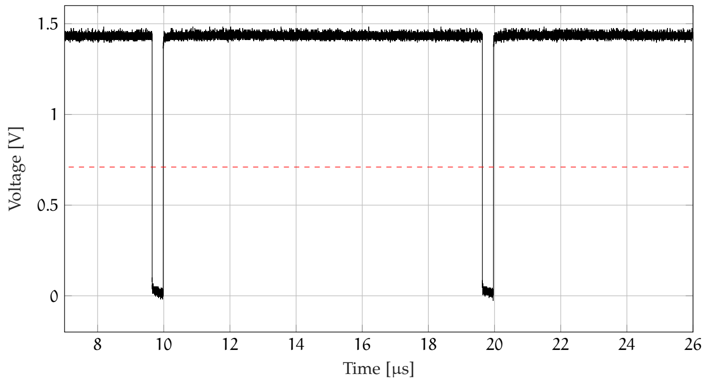


Figure 3.3: Sweep trigger of the SSOCT-1310 laser.

### 3.1.4 *Power profile*

Using a photodiode it's possible to measure the istantaneous power profile of the laser emission. The photodiode generates an electrical current which is proportional to the power of the detected electromagnetic field:

$$I_{ph} = \mathcal{R} \cdot P \tag{3.7}$$

The constant $\mathcal{R}$ is called *responsivity* [A/W] and is specific to the detector used. The current can then be measured with an oscilloscope. In order to avoid the saturation of the receiver, a 3 dB coupler was inserted between the source and the photodiode. The obtained power profile is depicted in Figure 3.4 along with the sweep trigger. We can observe that in the first $\sim 5$ μs after the positive edge of the trigger, the istantaneous power behaves like a typical laser pulse while outside of this interval it assumes an irregular profile.

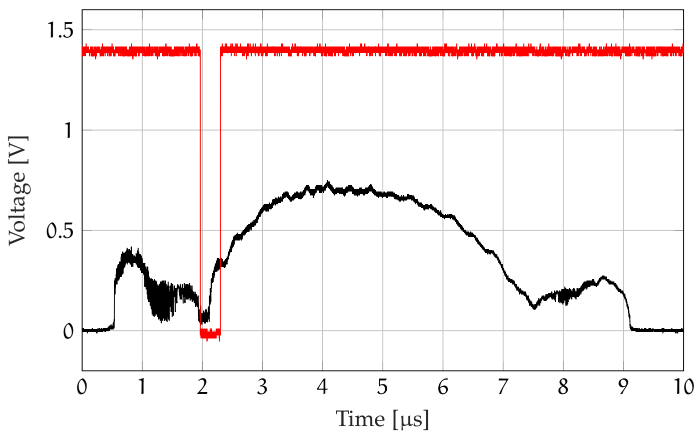


Figure 3.4: Sweep trigger of the SSOCT-1310 laser.

### 3.1.5 *k-clock*

As already stated, this particular SS-OCT laser is equipped with an internal MZI which generates the variable-frequency clock, called k-clock, used to sample the A-scan signal at a variable rate and equalize the nonlinear terms in the frequency sweep. As we can see in Figure 3.5, this signal assumes values in the $[0, 900]$ mV range with an average value of about 460 mV. This sinusoidal signal will be used to drive the acquisition board for the first 5 µseconds of the sweep and from this point forward will be referred to as *useful clock*. As per Table 3.1, the total number of samples that cab be acquired using this clock is $N_s = 1536$. In the last 5 µseconds the clock is called "dummy" because of its undefined behaviour that could lead to issues in the clocking of the DAQ devices.

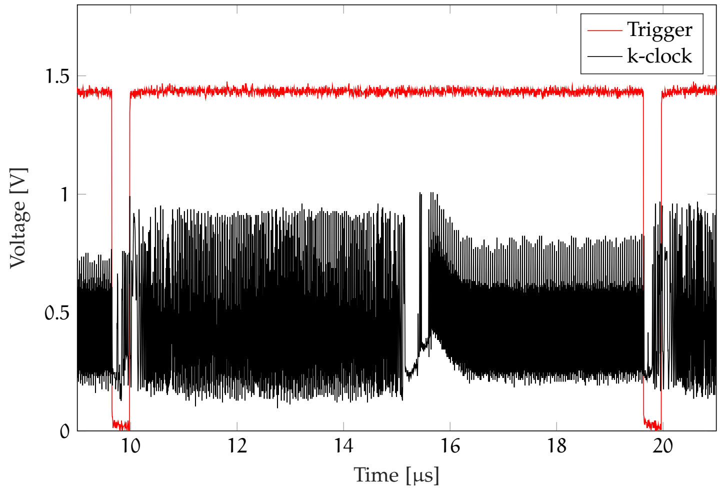


Figure 3.5: Estimate of the istantaneous frequency of the k-clock.

In Figure 3.6 are depicted two 50 nanoseconds windows at the start (left) and in the middle (right) of the useful clock, where the variable frequency of signal is clearly visible. Also worth noting is that at the start of the sweep the signal appears much more distorted than in the middle of the sweep. Fortunately, this behaviour did not compromise the performance of the system.

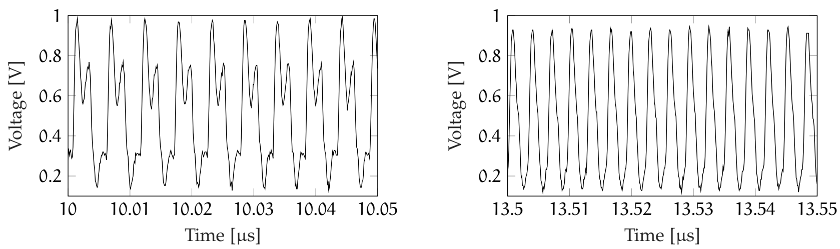


Figure 3.6: Behaviour of the useful k-clock at different time instants.

To gain further insights on the nature of the frequency sweep, it is interesting to estimate the istantaneous frequency of the k-clock. A method to perform this estimate is the following

1. Subtract the average value from the signal
2. Interpolate the signal $(t, y)$ to obtain $(\hat{t}, \hat{y})$
3. Determine the time instants $\hat{t}_i$ at which the signal $\hat{y}$ crosses 0, from which a vector $\mathcal{I} = \left[\hat{t}_{i_1}, \hat{t}_{i_2}, \ldots, \hat{t}_{i_N}\right]$ is built.
4. Compute the difference between the adjacent elements of $\mathcal{I}$ and obtain $\mathcal{T} = \left[\hat{\tau}_{i_1}, \hat{\tau}_{i_2}, \ldots, \hat{\tau}_{i_{N-1}}\right]$,
5. The istantaneous frequency of the signal is then estimated as $\hat{f}_i = 1/2\hat{\tau}_i$.

The result of this method is illustrated in Figure 3.7. Since the estimate is rather noisy, a low pass filter was applied to the $\hat{f}_i$ signal, resulting in a much cleaner estimation (depicted in red). As we can observe, the istantaneous frequency rapidly changes at the start and at the end of the sweep, while in the middle it stabilizes at about 320 MHz. Since a constant k-clock frequency implies a linear frequency sweep, we can infer that the sweep nonlinearities are much more prevalent at the edge of the sampling interval.

The maximum estimated frequency is $\hat{f}_{clk}^{max} = 339$ MHz, as opposed to the value that was reported in Table 3.1 of $f_{clk}^{max} = 332.2$ MHz. This slight overestimation is also visible in Figure 3.7, where we can see that the low-pass filtered signal is slightly higher than the average value of the non filtered one.

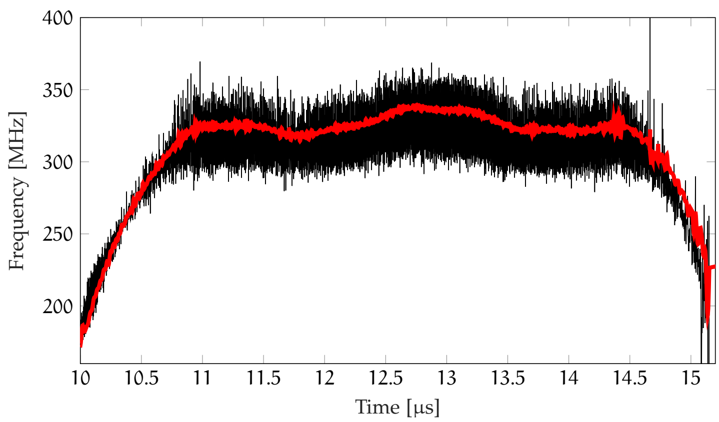


Figure 3.7: Estimate of the istantaneous frequency of the k-clock.

From the maximum frequency of the k-clock signal we can measure the maximum imaging depth obtainable by the system.

Two replicas of the pulse overlapping with a relative time delay $\tau$ will generate a beat frequency $f_b$ given by

$$f_b = \sigma_f \tau \tag{3.8}$$

where $\sigma_f$, the sweep speed, was determined in Equation 3.2. In a OCT setup, the time delay $\tau$ is related to the path mismatch of reference and sample arm, which in turn depends on the depth of the layer of the sample that generates the reflection. In this way

$$\tau = \frac{2dn}{c_0}, \tag{3.9}$$

where $c_0$ is the speed of light in vacuum, $n$ is the refractive index of the sample and $d$ is the depth. By the Nyquist theorem, the maximum beat frequency that can be digitized using the $k$-clock is

$$f_b^{max} = \frac{f_{clk}^{max}}{2}, \tag{3.10}$$

which results in a maximum depth in air ($n = 1$) of

$$d_{max} = \frac{c_0 f_b^{max}}{2\sigma_f} = \frac{c_0 f_{clk}^{max}}{4\sigma_f} \simeq 5.1 \text{ mm}. \tag{3.11}$$

### 3.1.6 *Coherence length*

In Chapter 2 we have seen that the coherence length of a source is one of the most important parameters of optical sources, independently of the type of OCT system. In TD-OCT, this parameter determines the axial resolution of the system, while FD-OCT schemes it also affects the imaging range, as the reference arm is fixed. In particular, complex conjugate artifacts arising from the Fourier trasform of the detected signals halve the maximum imaging range. For this reason, the coherence length of a swept source satisfies the following inequality

$$l_c \geqslant 2 \cdot d_{max}, \tag{3.12}$$

which implies that the coherence length of the SSOCT-1310 source is at least

$$l_c \geqslant 2 \cdot d_{max} \approx 10.2 \text{ mm}. \tag{3.13}$$

The exact value was experimentally determined in [9], measuring the normalized coherence function $|\gamma(\Delta z)|$ by placing a mirror in the sample arm and acquiring the interference signal for different values of OPD. The path length difference was changed by translating the reference mirror. The intensity of the interference signal, normalized by its maximum value, is plotted in Figure 3.8 as a function of the

OPD. When the OPD increases above a certain value, the coherence function decays exponentially as

$$|\gamma(\Delta z)| \propto e^{-\alpha|\Delta z|}, \tag{3.14}$$

which corresponds to a linear decay in the logarithmic domain. The parameter $\alpha$ was estimated by fitting the data points to a line using a Least-Squares fit. The coherence length is finally determined as the $\Delta z$ value such that $|\gamma(\Delta z)| = 1/2$, resulting in

$$l_c = 2 \cdot \frac{\ln 2}{\alpha} \approx 12.3 \text{ mm}. \tag{3.15}$$

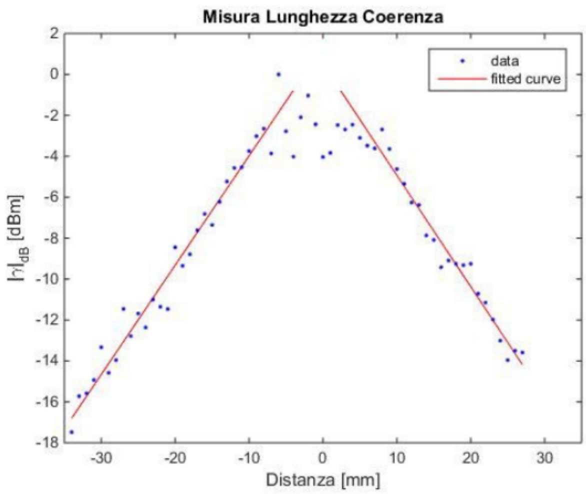


Figure 3.8: Experimental estimation of the normalized coherence function.

## 3.2 SCANNING SYSTEM

One of the most critical components of an OCT is the scanning system. Its role is to receive the light emitted by the source, focus it on the sample under test, and collect the backreflections. A scanning system usually comprises of three different devices

1. Fiber collimator
2. Galvanometric Mirrors
3. Focusing lens

A schematic of this system is depicted in Figure 3.9. Light coming from a single mode optical fiber is deflected by a system of galvanometric mirrors towards a lens which in turns focuses the radiation on the sample. By rotating the mirrors the light beam is focused on a different position on the sample. The reflected beam travels the same

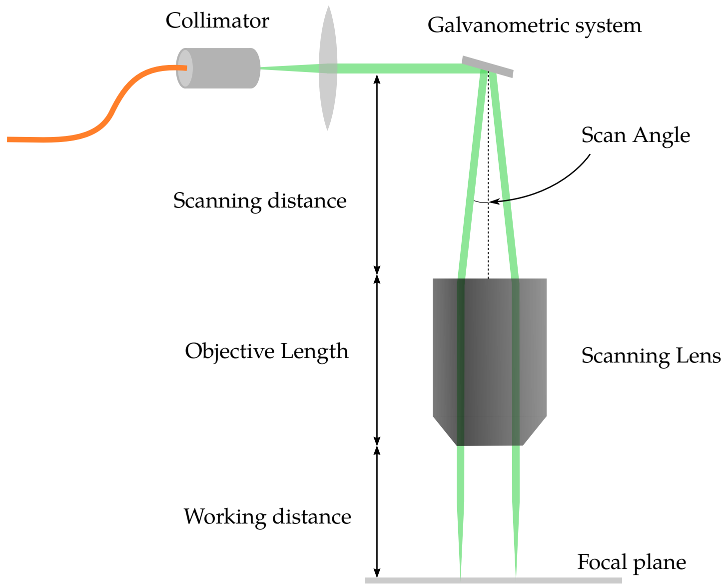


Figure 3.9: Diagram of a OCT scanning system.

path in the opposite direction and is collected by the optical fiber. The correct design of these components is paramount in order to guarantee small transversal and axial resolutions of the OCT system.

### 3.2.1 *Collimator*

The role of the fiber collimator is to collect light coming from a single mode fiber and collimate the beam on the galvanometric mirrors. The divergence angle at the output of the collimator is approximated with the following equation when the beams have a Gaussian intensity profile:

$$\theta \approx \frac{D}{f}\frac{180}{\pi}, \tag{3.16}$$

where D is the mode diameter and f is the focal length of the collimator. This approximation works well for sigle mode fibers, but will underestimate the real divergence angle in the case of multimode fibers, as the intensity profile has a non-Gaussian shape.

The collimator used in this setup is the Thorlabs F280APC-C[1], which is designed to work in the 1310 nm range. Its main specifications are summarized in Table 3.2.

### 3.2.2 *Scanning lens*

The light beam deviated by the galvanometric mirrors has to be focused on the sample under test in order to guarantee high resolution images. This is accomplished by a telecentric focusing lens. This type

1 https://www.thorlabs.com/thorproduct.cfm?partnumber=F280APC-C

| PARAMETER | UNITS | VALUE |
|---|---|---|
| Central wavelength | nm | 1310 |
| Beam diameter | mm | 3.4 |
| Divergence angle | degrees | 0.028 |
| Lens numerical aperture (NA) | – | 0.15 |
| Focal length | mm | 18.67 |

Table 3.2: Thorlabs F280APC-C datasheet.

of lenses is characterized by flat image planes which are ideal for OCT applications.

The main parameters that characterize this device are the following:

- Entrance Pupil Size (EP): it specifies the diameter of the collimated laser beam that will maximize the resolution of the imaging system. When using a single galvanometric mirror, the EP is located at the pivot point of the mirror. When two mirrors are used, the EP is located between the two mirrors.
- Scanning Distance (SD): the distance between the EP and the base of the lens.
- Scan Angle (SA): the angle between the incoming light beam and the optical axis of the lens.
- Working Distance (WD): the distance between the tip of the lens and the focal plane.
- Parfocal Distance (PD): the distance between the base of the lens and the focal plane. It is equal to the WD plus the objective length.
- Field of View (FOV): the area on the focal plane that can be imaged with a resolution equal or better than the one guaranteed by the lens.
- Depth of View (DOV): it corresponds to the distance between parallel planes on either side of the focal plane, where the beam spot diameter is $\sqrt{2}$ greater than it is at the focal plane. Using lenses with a high DOV value yields images with high lateral resolution in a larger interval of depths.
- Spot size: the diameter of the beam on the focal plane.

The lens used for the SS-OCT system developed in this thesis is the Thorlabs LSM04[2]. Its main specifications are listed in Table 3.3.

2 https://www.thorlabs.com/thorproduct.cfm?partnumber=LSM04

A simulation of the beam spot size on the focal plane is available in Figure 3.10, where we can see that it increases for bigger scan angles. This behaviour has the effect of reducing the lateral resolution at the edge of the FOV.

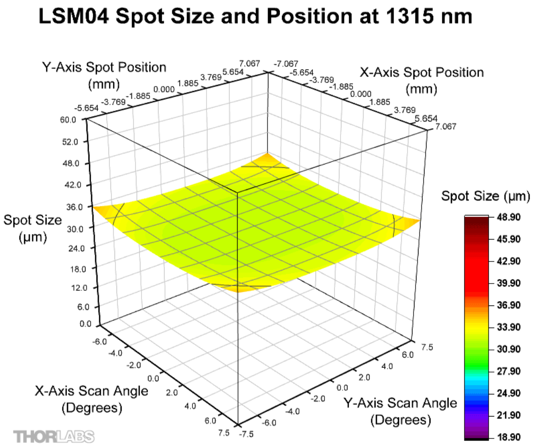


Figure 3.10: The Thorlabs GVS002 galvo system.

| PARAMETER | UNITS | VALUE |
|---|---|---|
| Wavelength range | nm | 1250-1380 |
| Effective Focal Length (EFL) | mm | 54 |
| Entrance Pupil size | mm | 4 |
| Working Distance | mm | 42.3 |
| Parfocal Distance | mm | 80.8 |
| Scan Distance | mm | 18.9 |
| Maximum Scan Angle | degrees | $\pm 7.5 \times \pm 7.5$ |
| Field of View | $mm^2$ | $14.1 \times 14.1$ |
| Depth of View | mm | 0.61 |

Table 3.3: Thorlabs LSM04 datasheet.

### 3.2.2.1 *Lateral resolution*

Using the parameters listed in Table 3.3 it is also possible to obtain an estimate of the lateral resolution of the system, which is dictated by the diffraction limited spot size of the focused optical beam. For Gaussian-shaped beams, it is approximated as [15]

$$\delta x \simeq \frac{4\lambda_0}{\pi} \frac{f}{d} \tag{3.17}$$

where $\lambda_0$ is the central wavelength of operation, $f$ is the focal length of the lens and $d$ is the diameter of the beam at the entrance of the lens. The lateral resolution guaranteed by the LSM04 is thus

$$\delta x \simeq \frac{4\lambda_0}{\pi}\frac{\mathsf{EFL}}{\mathsf{EP}} \approx 22.5\ \mu\text{m}. \tag{3.18}$$

Since the diameter of the beam exiting the fiber collimator is slightly smaller ($d = 3.4$ mm) than the EP size, the resulting lateral resolution becomes

$$\delta x \approx 26.5\ \mu\text{m}. \tag{3.19}$$

The depth of view, also called confocal parameter, limits the imaging depth of the system. Due to diffraction, this paramer is also governed by the lateral resolution of the system through the following equation

$$b = \frac{2\delta x^2}{\lambda_0}. \tag{3.20}$$

This effect is illustrated in Figure 3.11, where we can observe that using lenses with a high numerical aperture (NA), or small spot size, the depth of view is limited. In OCT systems it is preferred to use low NA lenses to sacrifice lateral resolution in favor of a depth of view comparable to the coherence length of the source. Following this criterion the coherence length is fully exploited.

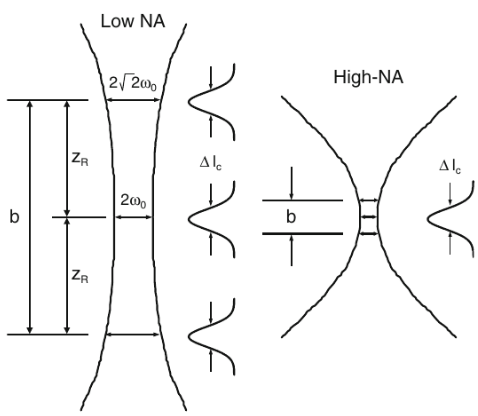


Figure 3.11: Basic diagram of a SS-OCT setup

Using the EP size the confocal parameter is $b \approx 0.61$ mm, equal to the value reported in Table 3.3, while using the beam size diameter $d = 3.4$ mm it becomes $b \approx 0.84$ mm.

### 3.2.3 *Galvanometric Mirrors*

In order to acquire B-scans and C-scans it is necessary to direct the laser beam emitted from the swept laser over a speficied area of the sample. This is accomplished by using a system of *galvanometric mirrors*, also called *galvo mirrors*. A cross-sectional image can be generated with a single 1D mirror, that is, a mirror which can rotate on a single axis, while volumetric data require the use of either a 2D mirror or a couple of 1D mirrors. In the second case, each mirror is responsible for the movement of the beam over a single direction on the focal plane, typically called X and Y.

Figure 3.12: The Thorlabs GVS002 galvo system.

The galvo system employed in this thesis work is the Thorlabs GVS002[3], which consists in two 1D silver plated mirrors, the motors that controls them, a detector to measure the mirrors' position and the servo driver boards that interpret the error signals coming from the detector to correctly drive the motors to the demanded position. A photo of the dual axis motor/mirror assembly is available in Figure 3.12. A thorough analysis of the electrical circuitry of the system is found in [9].

#### 3.2.3.1 *Controlling the mirrors*

The position of each mirror is controlled by sending a voltage signal to the respective driver board which is proportional to the mechanical angle of the respective motor. The maximum mechanical scan angle that the GVS002 system can handle is $\pm 12.5°$, but it can vary depending on the laser beam diameter and the voltage scaling factor. This particular galvo system offers three different scaling factors which also govern the maximum input voltage applied to the servo boards:

| SCALING FACTOR | MAX. VOLTAGE | MAX. SCAN ANGLE |
|---|---|---|
| 0.5 V/° | ±6.25 V | ±12.5° |
| 0.8 V/° | ±10 V | ±12.5° |
| 1 V/° | ±10 V | ±10° |

The scan angle seen by the focusing lens, called *optical scan angle*, $\theta_o$, is twice the mechanical scan angle applied to the mirror, $\theta_m$. Set-

3 https://www.thorlabs.com/thorproduct.cfm?partnumber=GVS002

ting the scaling factor $\alpha = 1\mathrm{V}/°$, the maximum optical scan angle then becomes $\pm 20°$, which allows us fully exploit the maximum angle supported by the lens. In this case, the full FOV is scanned if the applied voltage is $v_{max} = \pm 7.5°/(2\alpha) = \pm 3.75$ V.

The beam spot position on the focal plane is related to the mechanical angle applied to the mirrors and the focal length of the lens through the following relation

$$x = \mathrm{EFL}\tan(2\theta_{m,x}) \tag{3.21}$$
$$y = \mathrm{EFL}\tan(2\theta_{m,y}) \tag{3.22}$$

With a scaling factor equal to $\alpha$, the voltage signal $v_{x,y}(t)$ will therefore focus the beam at the following position

$$x(t) = \mathrm{EFL}\tan\left[2\alpha_s v_x(t)\frac{\pi}{180}\right] \tag{3.23}$$
$$y(t) = \mathrm{EFL}\tan\left[2\alpha_s v_y(t)\frac{\pi}{180}\right] \tag{3.24}$$

The two signals $v_x$ and $v_y$ are delivered to the driver boards as two pairs of positive voltage signals, $(v_x^+, v_x^-)$ and $(v_y^+, v_y^-)$.

#### 3.2.3.2 *Image distortion*

When using a two-mirror system three different effects can appear

1. The arrangement of the mirrors leads to a distortion of the image field, which will be "pillow-shaped" instead of rectangular (fig:galvo-distortion). This is due to the fact that the distance between the two mirrors depends on the mechanical angle applied to the mirrors.

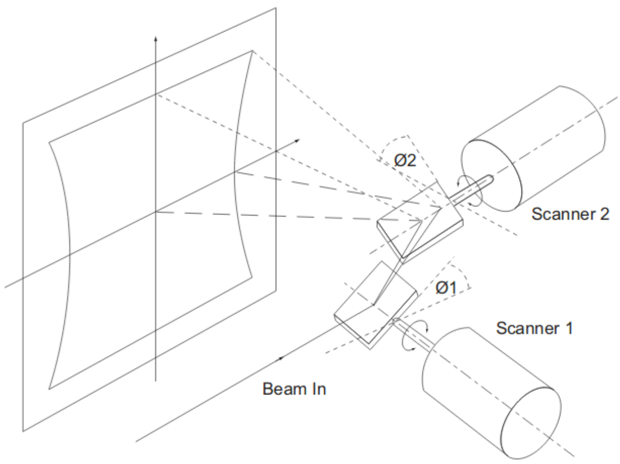


Figure 3.13: Field distortion using two mirrors.

2. From Equation 3.21 and Equation 3.22 we can observe that the distance on the image field is not directly proportional to the

applied angle but to its tangent. This can result in an additional distortion effect.

3. If an ordinary lens is used for focusing the laser beam, the focus lies on a sphere. In a flat image field, a varying spot size results.

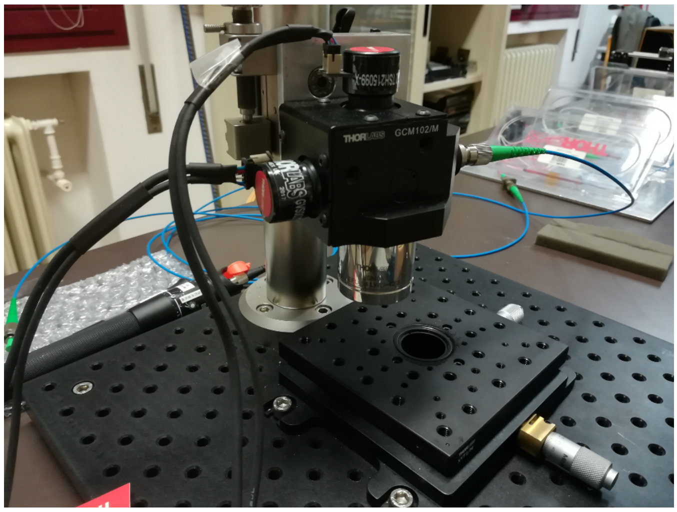

Figure 3.14: The final scanning system mounted on a movable vertical support.

## 3.3 ACQUISITION BOARD

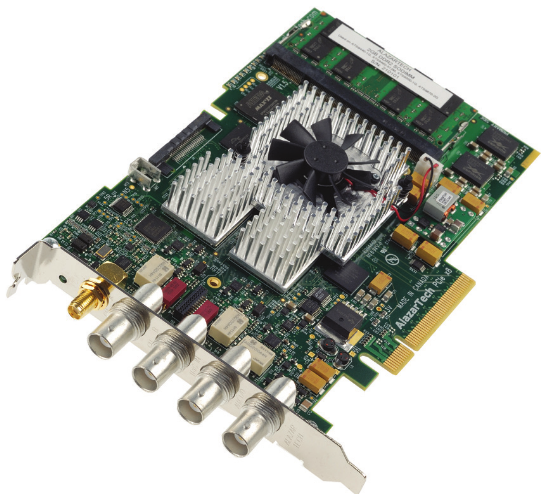

Figure 3.15: The acquisition board, AlazarTech ATS9350.

### 3.3.1

In Figure 3.16 a comparison between the two acquisition techniques is available. For Single-port Acquisitions, in Figure 3.16b we can see that

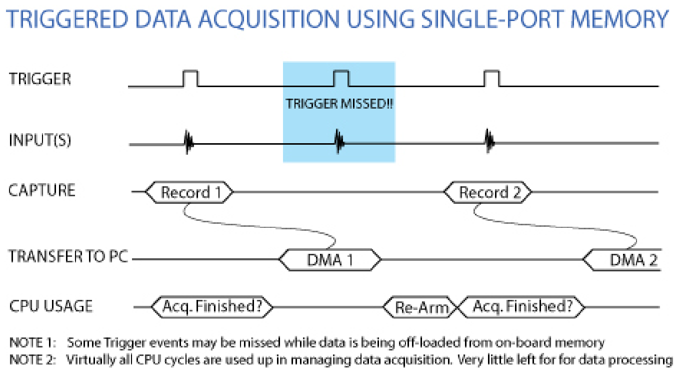


(a) Acquisition using Single-Port Memory.

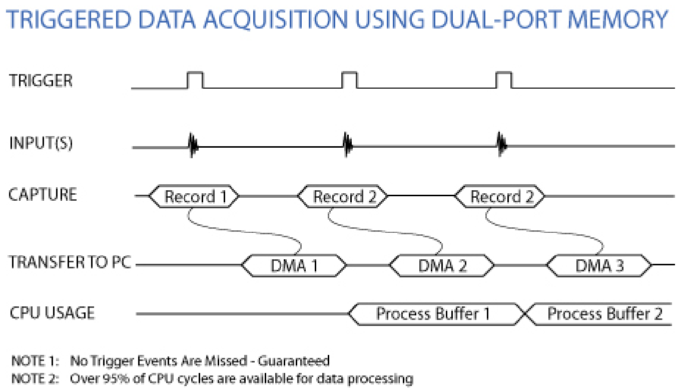


(b) Acquisition using Dual-Port Memory.

Figure 3.16: Diagram highlighting the differences between Sigle-Port acqusitions and Dual-Port acqusitions

no trigger events are missed and over 95% of CPU time is available for data processing, while in Figure 3.16a trigger events happening while the DMA transfer is ongoing are missed completely, and virtually all CPU cycles are used in managing the data acquisition. This leaves no room for data processing on the CPU.

## 3.4 OPTICAL CIRCUIT

### 3.4.1 *Mach-Zender Interferometer*

In order to test the k-clock and the acquisition device blah blah blah used AlazarDSO softeare to obtani the beating signal of unbalanced MZI -> show difference also on images

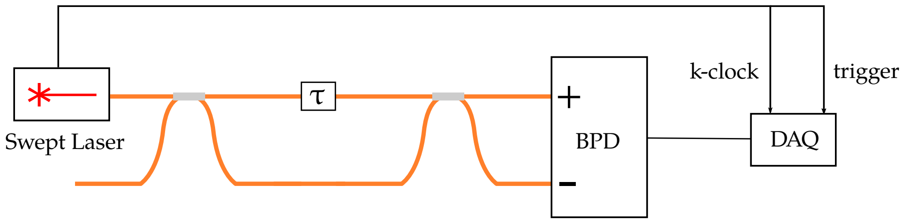


Figure 3.17: Diagram of an unbalanced Mach-Zender Interferometer.

### 3.4.2 *Basic setup and Stability Analysis*

### 3.4.3 *Final Setup with OBR balancing*

Add couplers length measurements; focus in the middle of the imaging range.

### 3.4.4 *Axial Resolution*

Try with new measurements

### 3.4.5 *Thickness measurements*

No scattering detected, only reflections caused by the surface

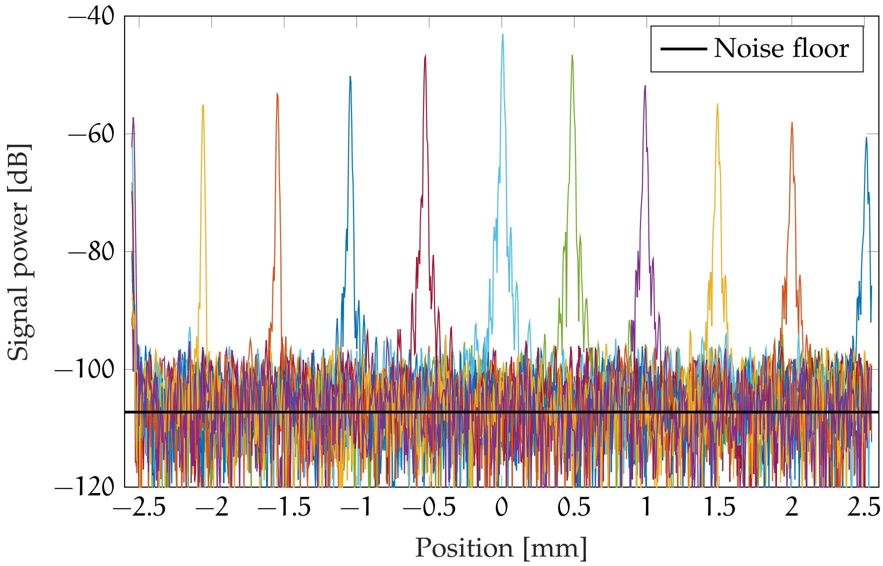


Figure 3.18: Signal spectrum at various depths.

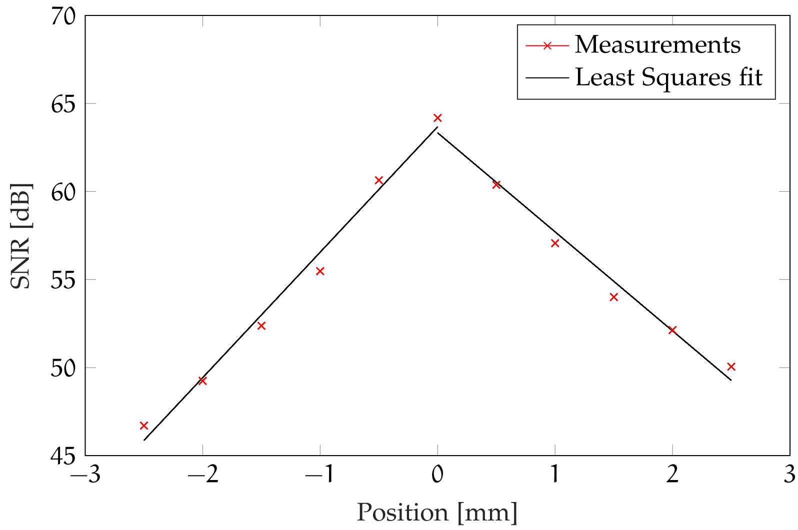


Figure 3.19: Signal-to-noise ratio falloff.

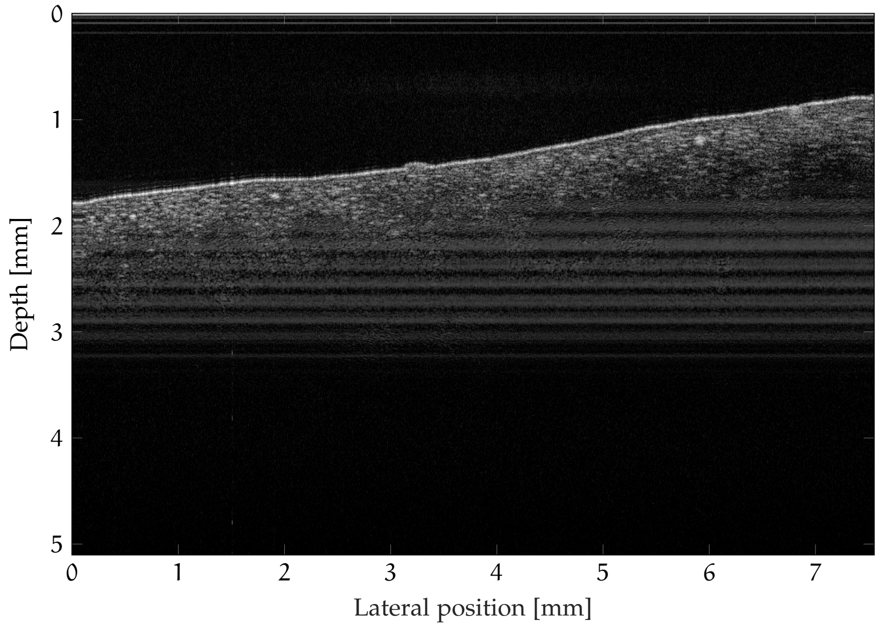


Figure 3.20: B-scan of banana peel.

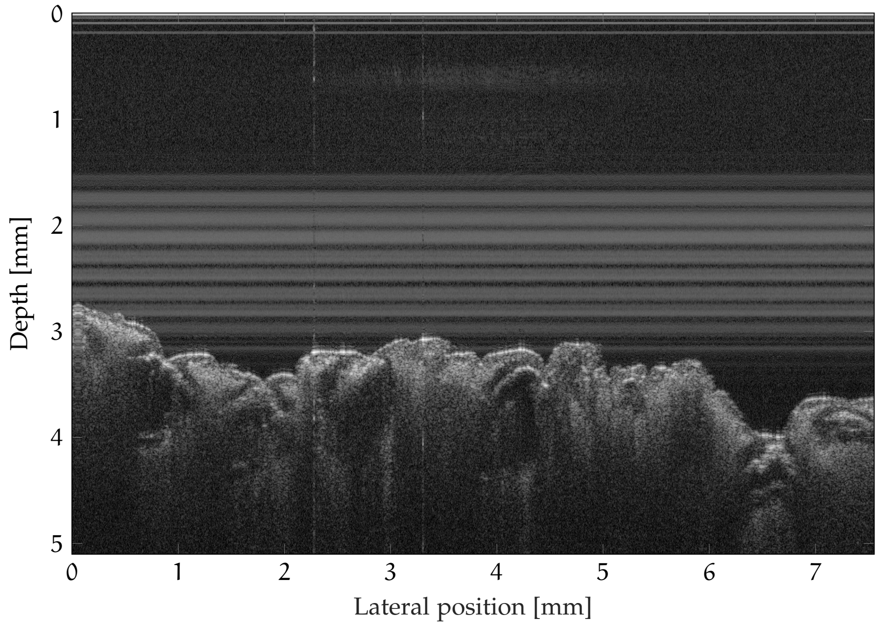


Figure 3.21: B-scan of dry orange peel.

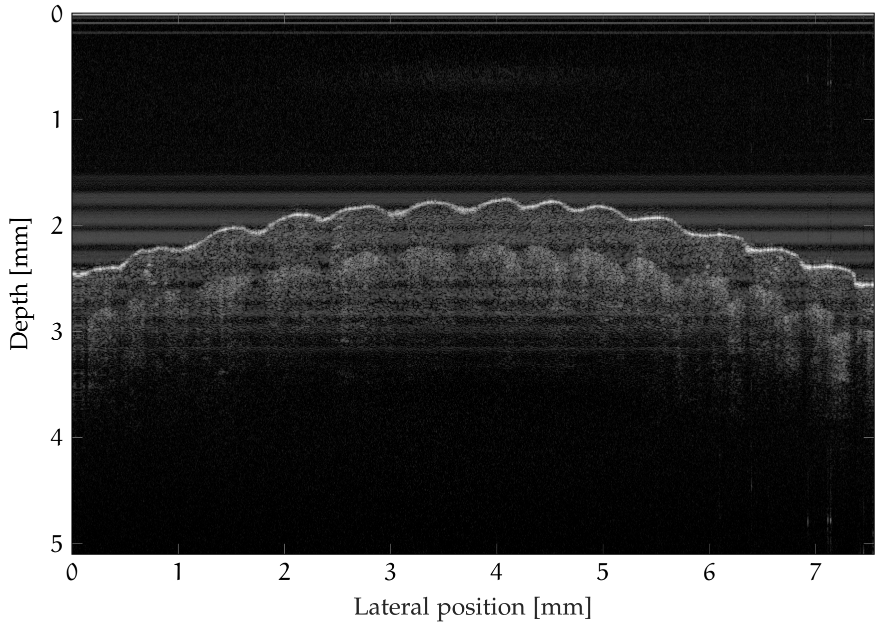


Figure 3.22: B-scan of a human finger.

# 4 RESULTS

## 4.1 Data acquisition software

Leave this chapter for the explanation of the software, technologies used, performance achieved and showcase of the measurements. B-scans, volumes and enface. Also include control of the galvo mirrors in here since it's about C++ programming.

### 4.1.1 *Digital Signal Processing Chain for OCT*

### 4.1.2 *The Qt programming framework*

## 4.2 The signal-slot paradigm

Blocking vs Non-blocking calls

### 4.2.1 *Displaying graphics with OpenGL*

### 4.2.2 *Parallel Computing with OpenMP*

OpenMP[1] is a multi-platform *Application Programming Interface* (API) for shared-memory parallel processing programming available for various programming languages, such as C, C++ and Fortran.

*OpenMP stands for Open **M**ulti-**P**rocessing*

## 4.3 Basic setup

#### 4.3.0.1 *Stability Analysis*

### 4.3.1 *New setup*

### 4.3.2 *Balancing the optical paths*

#### 4.3.2.1 *Working mechanism of a OBR*

#### 4.3.2.2 *Measuring path lengths*

### 4.3.3 *Axial Resolution*

resolution = minimum distance at which two objects are distinguishable NOT absolute position of an object. Also explain that worse re-

1 http://www.openmp.org/

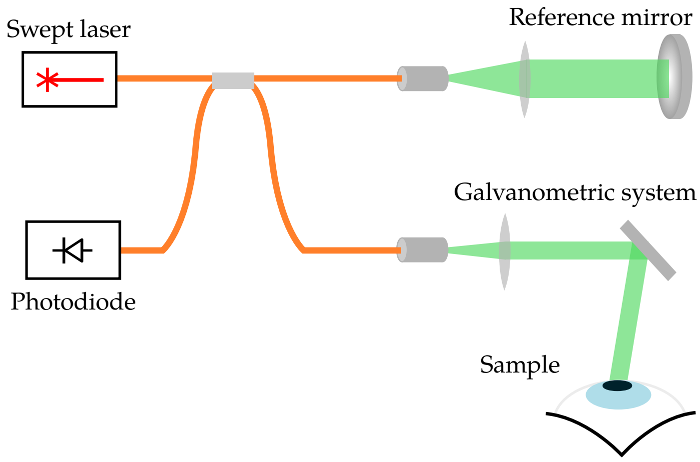


Figure 4.1: Basic diagram of a SS-OCT setup

sult than theoretical might be explained by dispersion in the system and the use of a SMF patch coord designed for 1550nm range.

### 4.3.4 *Axial Measurements*

### 4.3.5 *Amplified Photodiode*

Content

## 4.4 GALVANOMETRIC SYSTEM CONTROL

1. NI-DAQmx framework
2. C programming
3. Triggering and Clocking
4. Splitting Positive and Negative voltages
5. Conversion from volts to angles to surface area
6. Trigger enable
7. X-Motor -> Triangle Wave
8. Y-Motor -> Staircase for C-scans

## 4.5 USAF TARGET

1. What it is
2. How it works
3. Acquisitions in different conditions

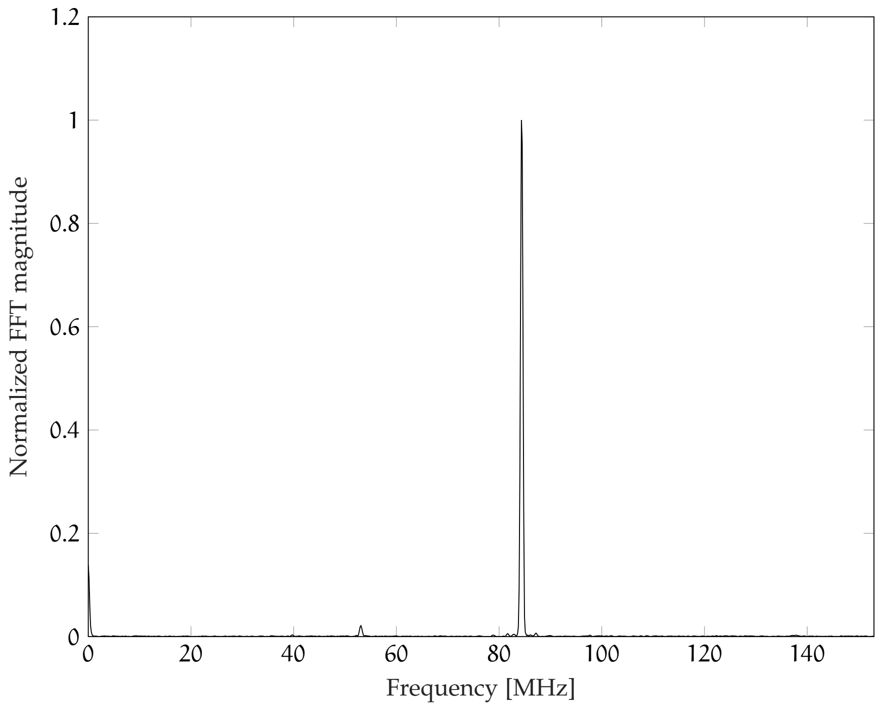


Figure 4.2: Beat frequency generated by the unbalanced MZI, sampled with the internal 500MS/s clock.

4. B-scans

5. Surface images -> verifying transverse resolution

Content

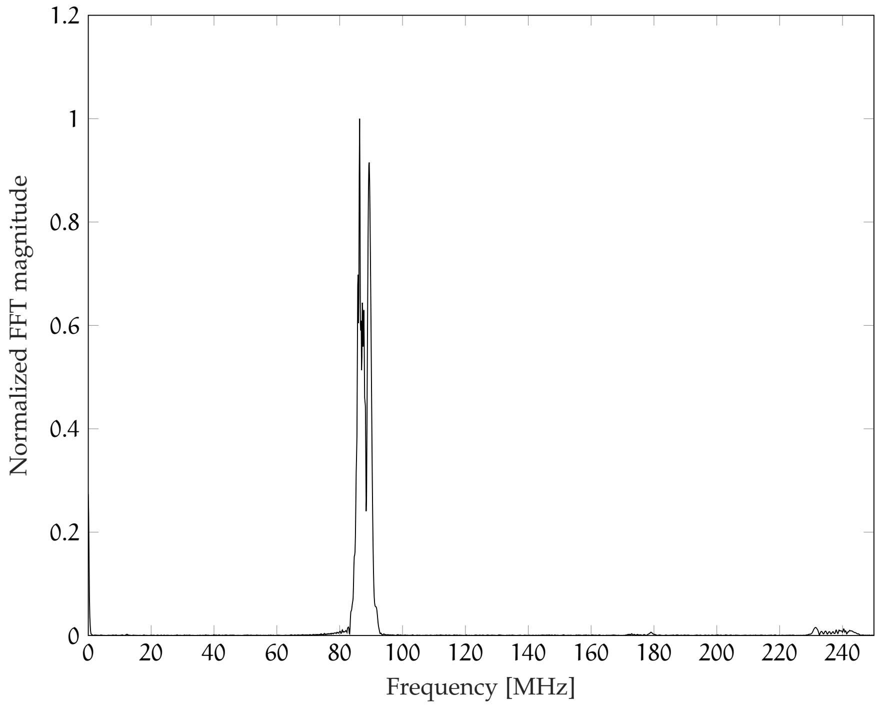


Figure 4.3: Beat frequency generated by the unbalanced MZI, sampled with the external k-clock.

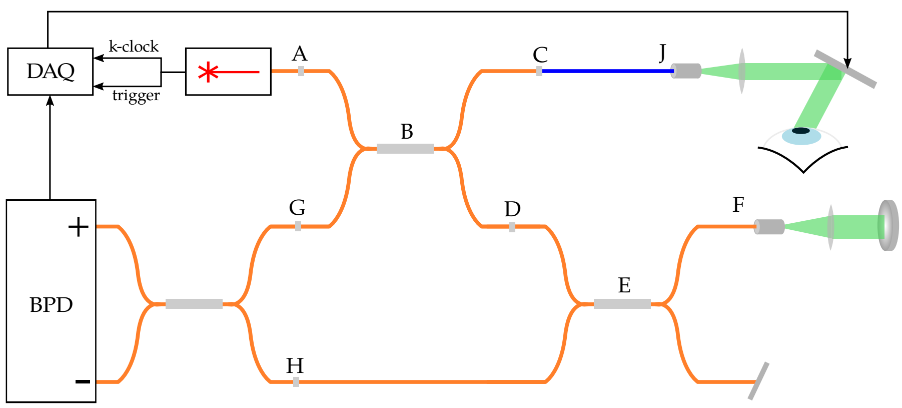


Figure 4.4: Final SS-OCT setup.

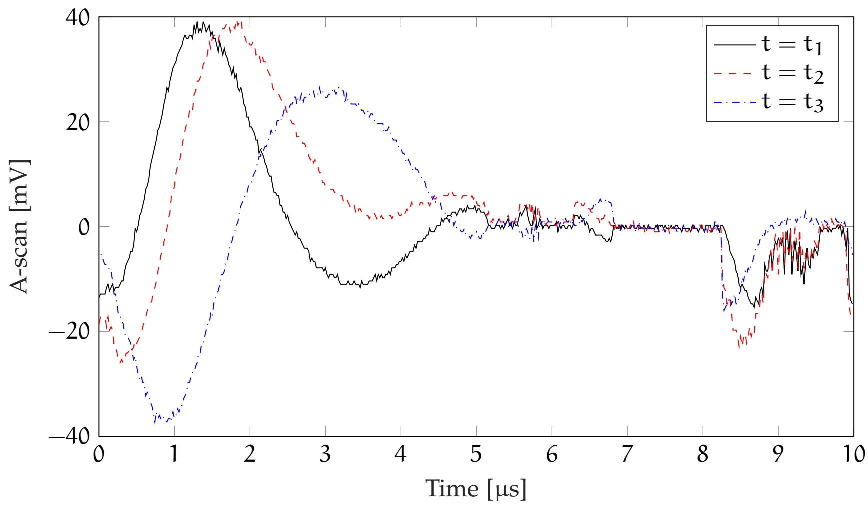


Figure 4.5: Time signal when the optical path difference is close to 0.

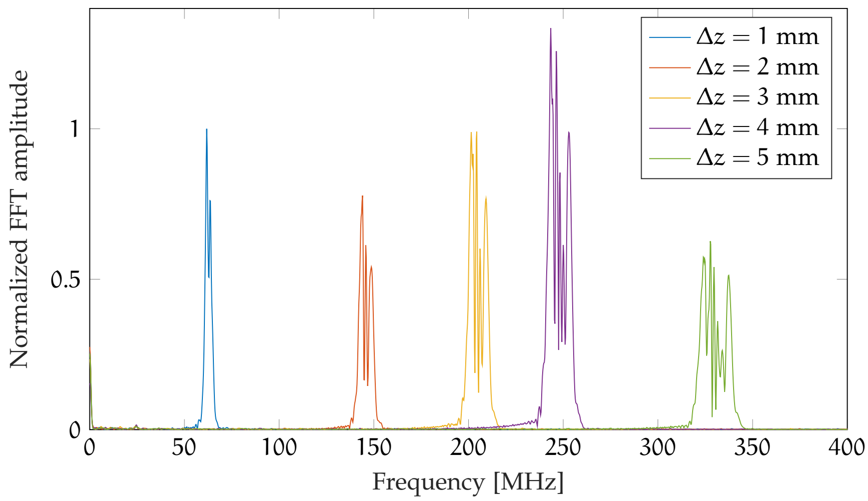


Figure 4.6: Effect of reference arm unbalancing on the beat frequency

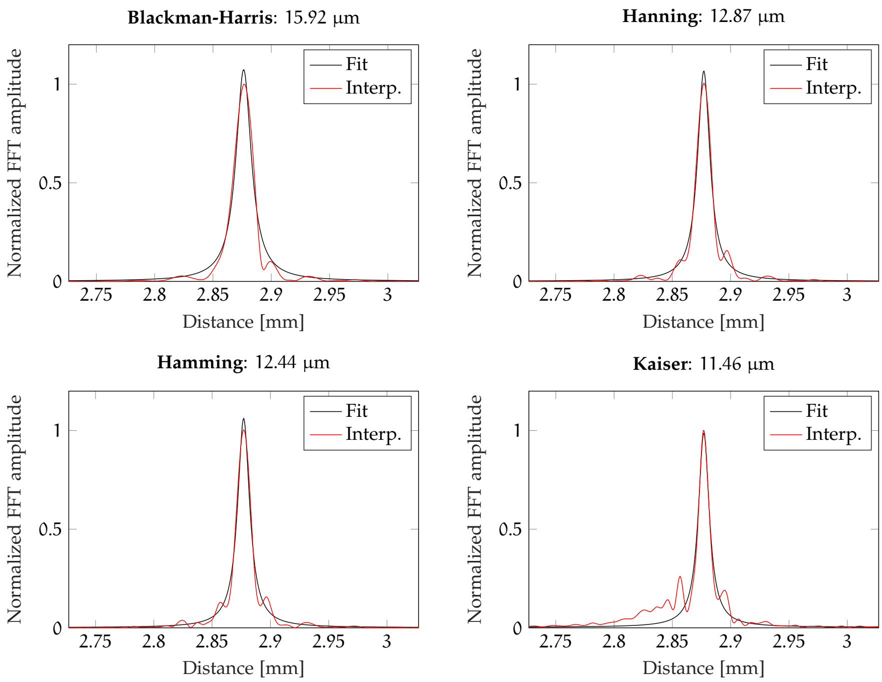


Figure 4.7: Estimate of the axial resolution with Lorentzian curve fitting. Nonlinear least squares. $y_0 = 0.0009$, $x_c = 2.8763$, $A = 0.0268$, $w = 0.0159$

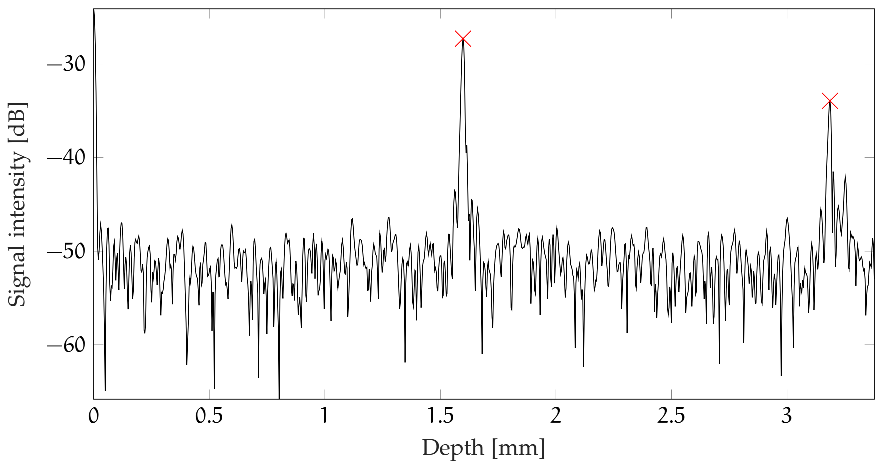


Figure 4.8: Axial measurement of the USAF target.

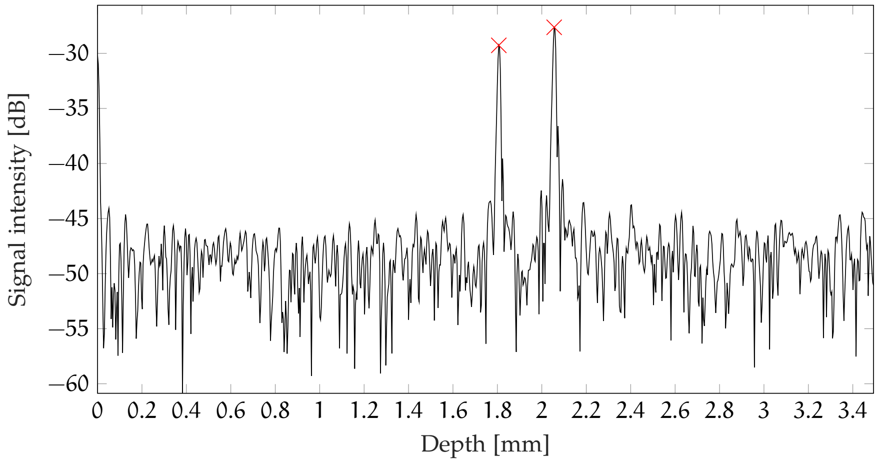


Figure 4.9: Axial measurement of an optical fiber.

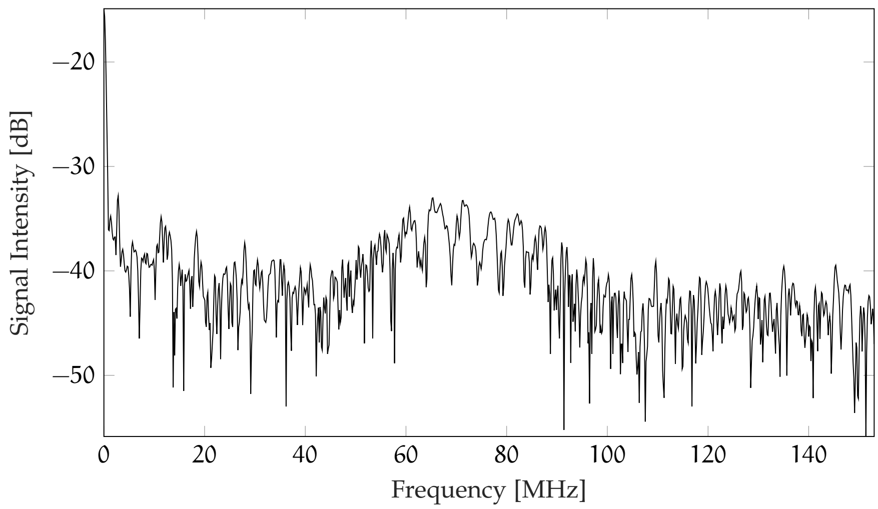


Figure 4.10: Spurious beat frequencies detected by the Exalos BPD.

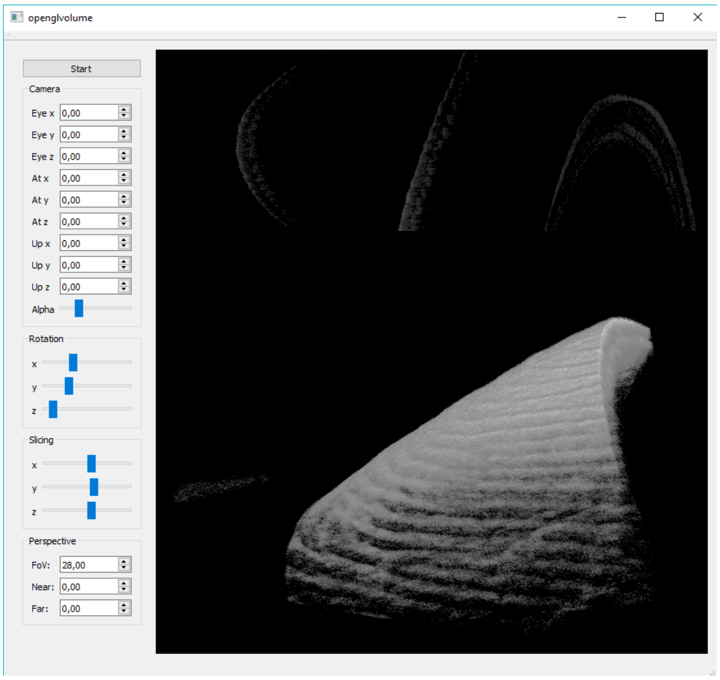


Figure 4.11: 3D rendering of a human finger.

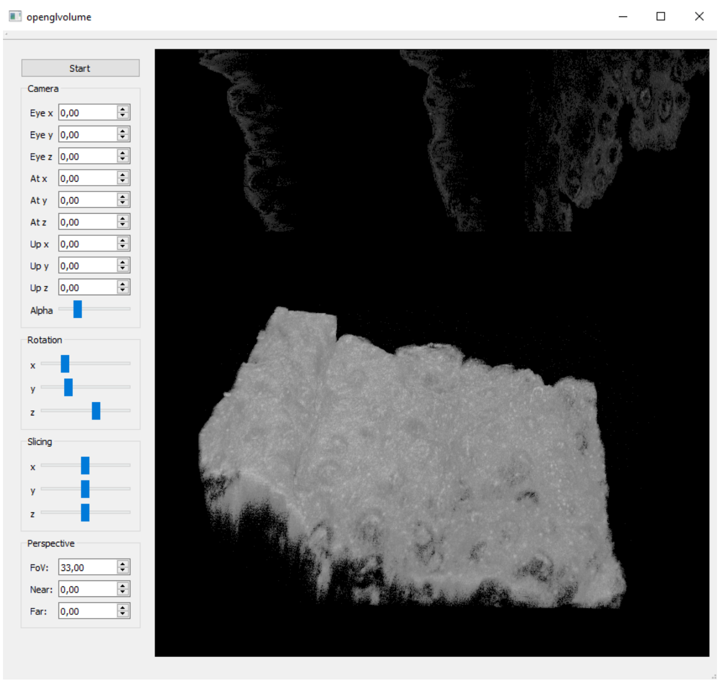


Figure 4.12: 3D rendering of a human finger.

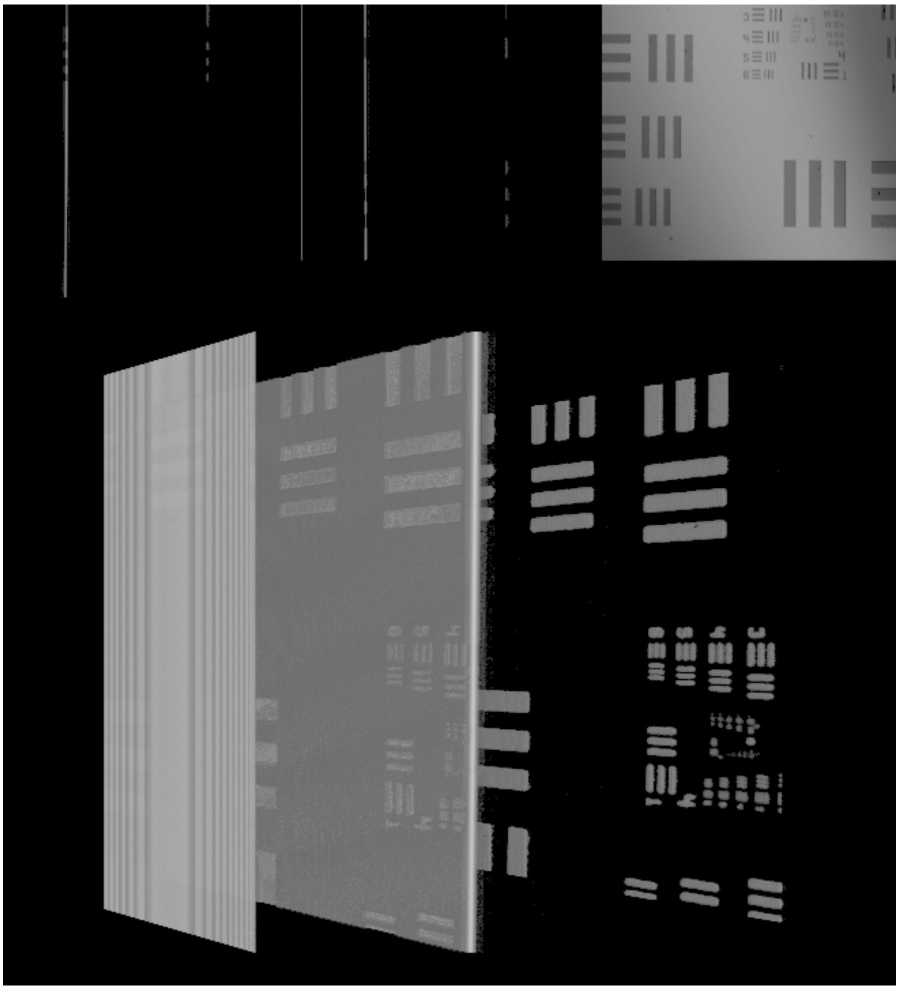

Figure 4.13: 3D rendering of the USAF target

# 5 CONCLUSIONS

# Part I

# APPENDIX

# A APPENDIX TEST

## A.1 APPENDIX SECTION TEST

## A.2 ANOTHER APPENDIX SECTION TEST

*More dummy text*

There is also a useless Pascal listing below: Listing A.1.

| LABITUR BONORUM PRI NO | QUE VISTA | HUMAN |
|---|---|---|
| fastidii ea ius | germano | demonstratea |
| suscipit instructior | titulo | personas |
| quaestio philosophia | facto | demonstrated |

Table A.1: Autem usu id.

Listing A.1: A floating example (`listings` manual)

```
for i:=maxint downto 0 do
begin
{ do nothing }
end;
```

[1] Erkki Alarousu, Leszek Krehut, Tuukka Prykäri, and Risto Myllylä. «Study on the use of optical coherence tomography in measurements of paper properties.» In: *Measurement Science and Technology* 16.5 (2005), p. 1131. URL: http://stacks.iop.org/0957-0233/16/i=5/a=012.

[2] B. T. Amaechi, S. M. Higham, A. GH. Podoleanu, J. A. Rogers, and D. A. Jackson. «Use of optical coherence tomography for assessment of dental caries: quantitative procedure.» In: *Journal of Oral Rehabilitation* 28.12 (2001), pp. 1092–1093. ISSN: 0305-182X. DOI: 10.1046/j.1365-2842.2001.00840.x. URL: http://doi.wiley.com/10.1046/j.1365-2842.2001.00840.x.

[3] Johannes F. de Boer, Thomas E. Milner, Martin J. C. van Gemert, and J. Stuart Nelson. «Two-dimensional birefringence imaging in biological tissue by polarization-sensitive optical coherence tomography.» In: *Optics Letters* 22.12 (1997), p. 934. ISSN: 0146-9592. DOI: 10.1364/OL.22.000934. URL: https://www.osapublishing.org/abstract.cfm?URI=ol-22-12-934.

[4] Stephen A. Boppart, Juergen Herrmann, Costas Pitris, Debra L. Stamper, Mark E. Brezinski, and James G. Fujimoto. «High-Resolution Optical Coherence Tomography-Guided Laser Ablation of Surgical Tissue.» In: *Journal of Surgical Research* 82.2 (1999), pp. 275–284. ISSN: 00224804. DOI: 10.1006/jsre.1998.5555. URL: http://linkinghub.elsevier.com/retrieve/pii/S002248049895555X.

[5] Stephen A. Boppart, Wei Luo, Daniel L. Marks, and Keith W. Singletary. «Optical Coherence Tomography: Feasibility for Basic Research and Image-guided Surgery of Breast Cancer.» In: *Breast Cancer Research and Treatment* 84.2 (2004), pp. 85–97. ISSN: 1573-7217. DOI: 10.1023/B:BREA.0000018401.13609.54. URL: https://doi.org/10.1023/B:BREA.0000018401.13609.54.

[6] Max Born, Emil Wolf, A. B. Bhatia, P. C. Clemmow, D. Gabor, A. R. Stokes, A. M. Taylor, P. A. Wayman, and W. L. Wilcock. *Principles of Optics: Electromagnetic Theory of Propagation, Interference and Diffraction of Light*. 7th ed. Cambridge University Press, 1999. DOI: 10.1017/CBO9781139644181.

[7] B E Bouma et al. «Evaluation of intracoronary stenting by intravascular optical coherence tomography.» In: *Heart* 89.3 (2003), pp. 317–320. ISSN: 1355-6037. DOI: 10.1136/heart.89.3.317. eprint: http://heart.bmj.com/content/89/3/317.full.pdf. URL: http://heart.bmj.com/content/89/3/317.

[8] Brian Cabral, Nancy Cam, and Jim Foran. «Accelerated Volume Rendering and Tomographic Reconstruction Using Texture Mapping Hardware.» In: *Proceedings of the 1994 symposium on Volume visualization - VVS '94*. New York, New York, USA: ACM Press, 1994, pp. 91–98. ISBN: 0897917413. DOI: 10.1145/197938.197972. URL: http://portal.acm.org/citation.cfm?doid=197938.197972.

[9] Marco Calabrese. «Progetto di un Tomografo a Coerenza Ottica ad Alta Velocità.» MA thesis. Dipartimento di Ingegneria dell'Informazione, Padova (Italy): Università degli Studi di Padova, 2017.

[10] Dong-hak Choi, Hideaki Hiro-Oka, Kimiya Shimizu, and Kohji Ohbayashi. «Spectral domain optical coherence tomography of multi-MHz A-scan rates at 1310 nm range and real-time 4D-display up to 41 volumes/second.» In: *Biomedical Optics Express* 3.12 (2012), p. 3067. ISSN: 2156-7085. DOI: 10.1364/BOE.3.003067. URL: https://www.osapublishing.org/abstract.cfm?URI=boe-3-12-3067.

[11] Tzu H. Chow, Khay M. Tan, Beng K. Ng, Sirajudeen G. Razul, Chia M. Tay, Tet F. Chia, and Wee T. Poh. «Diagnosis of virus infection in orchid plants with high-resolution optical coherence tomography.» In: *Journal of Biomedical Optics* 14.1 (2009), p. 014006. ISSN: 10833668. DOI: 10.1117/1.3066900. URL: http://biomedicaloptics.spiedigitallibrary.org/article.aspx?doi=10.1117/1.3066900.

[12] Seyed Hamid Hosseiny Darbrazi. «GPU-Accelerated Optical Coherence Tomography Signal Processing and Visualization.» PhD thesis. Universidade do Porto, 2016.

[13] Anjul M. Davis, Michael A. Choma, and Joseph A. Izatt. «Heterodyne swept-source optical coherence tomography for complete complex conjugate ambiguity removal.» In: *Journal of Biomedical Optics* 10.6 (2005), p. 064005. ISSN: 10833668. DOI: 10.1117/1.2136147. URL: http://biomedicaloptics.spiedigitallibrary.org/article.aspx?doi=10.1117/1.2136147.

[14] Al-Hafeez Dhalla, Derek Nankivil, and Joseph a. Izatt. «Complex conjugate resolved heterodyne swept source optical coherence tomography using coherence revival.» In: *Biomedical Optics Express* 3.3 (2012), p. 633. ISSN: 2156-7085. DOI: 10.1364/BOE.3.000633.

[15] Wolfgang Drexler and James G. Fujimoto, eds. *Optical Coherence Tomography*. Cham: Springer International Publishing, 2015. ISBN: 978-3-319-06418-5. DOI: 10.1007/978-3-319-06419-2. URL: http://link.springer.com/10.1007/978-3-319-06419-2.

[16] Klaus Engel, Martin Kraus, and Thomas Ertl. «High-quality pre-integrated volume rendering using hardware-accelerated pixel shading.» In: *Proceedings of the ACM SIGGRAPH/EUROGRAPHICS workshop on Graphics hardware - HWWS '01*. New York, New York, USA: ACM Press, 2001, pp. 9–16. ISBN: 158113407X. DOI: 10.1145/383507.383515. URL: http://portal.acm.org/citation.cfm?doid=383507.383515.

[17] P. F. Escobar, J. L. Belinson, A. White, N. M. Shakhova, F. I. Feldchtein, M. V. Kareta, and N. D. Gladkova. «Diagnostic efficacy of optical coherence tomography in the management of preinvasive and invasive cancer of uterine cervix and vulva.» In: *International Journal of Gynecological Cancer* 14.3 (2004), pp. 470–474. ISSN: 1048-891X. DOI: 10.1111/j.1048-891x.2004.14307.x. URL: http://doi.wiley.com/10.1111/j.1048-891x.2004.14307.x.

[18] Daniel Fried, John Xie, Sahar Shafi, John D. B. Featherstone, Thomas M. Breunig, and Charles Le. «Imaging caries lesions and lesion progression with polarization sensitive optical coherence tomography.» In: *Journal of Biomedical Optics* 7.4 (2002), p. 618. ISSN: 10833668. DOI: 10.1117/1.1509752. URL: http://biomedicaloptics.spiedigitallibrary.org/article.aspx?doi=10.1117/1.1509752.

[19] J G Fujimoto, C a Puliafito, R Margolis, A Oseroff, S De Silvestri, and E P Ippen. «Femtosecond optical ranging in biological systems.» In: *Optics Letters* 11.3 (1986), p. 150. ISSN: 0146-9592. DOI: 10.1364/OL.11.000150. URL: https://www.osapublishing.org/abstract.cfm?URI=ol-11-3-150.

[20] G. Loeb and J. K. Barton. «Imaging Botanical Subjects With Optical Coherence Tomography: A Feasibility Study.» In: *Transactions of the ASAE* 46.6 (2003), pp. 1751–1757. ISSN: 2151-0059. DOI: 10.13031/2013.15616. URL: http://elibrary.asabe.org/abstract.asp??JID=3{\&}AID=15616{\&}CID=t2003{\&}v=46{\&}i=6{\&}T=1.

[21] T Gambichler, G Moussa, M Sand, D Sand, P Altmeyer, and K Hoffmann. «Applications of optical coherence tomography in dermatology.» In: *Journal of Dermatological Science* 40.2 (2005), pp. 85–94. ISSN: 09231811. DOI: 10.1016/j.jdermsci.2005.07.006. URL: http://linkinghub.elsevier.com/retrieve/pii/S092318110500201X.

[22] Alexandre R. Hariri Lidaand Tumlinson, David G. Besselsen, Urs Utzinger, Eugene W. Gerner, and Jennifer K. Barton. «Endoscopic optical coherence tomography and laser-induced fluorescence spectroscopy in a murine colon cancer model.» In: *Lasers in Surgery and Medicine* 38.4 (2006), pp. 305–313. ISSN: 0196-8092.

DOI: 10.1002/lsm.20305. URL: http://doi.wiley.com/10.1002/lsm.20305.

[23] David Huang et al. «Optical Coherence Tomography HHS Public Access.» In: *Science. November* 22.2545035 (1991), pp. 1178–1181. ISSN: 0036-8075. DOI: 10.1002/jcp.24872.The. arXiv: 15334406.

[24] Ik-Kyung Jang et al. «Visualization of coronary atherosclerotic plaques in patients using optical coherence tomography: comparison with intravascular ultrasound.» In: *Journal of the American College of Cardiology* 39.4 (2002), pp. 604–609. ISSN: 0735-1097. DOI: 10.1016/S0735-1097(01)01799-5. eprint: http://www.onlinejacc.org/content/39/4/604.full.pdf. URL: http://www.onlinejacc.org/content/39/4/604.

[25] Yali Jia et al. «Quantitative Optical Coherence Tomography Angiography of Choroidal Neovascularization in Age-Related Macular Degeneration.» In: *Ophthalmology* 121.7 (2014), pp. 1435–1444. ISSN: 01616420. DOI: 10.1016/j.ophtha.2014.01.034. URL: http://linkinghub.elsevier.com/retrieve/pii/S0161642014001043.

[26] Vrushali R. Korde et al. «Using optical coherence tomography to evaluate skin sun damage and precancer.» In: *Lasers in Surgery and Medicine* 39.9 (2007), pp. 687–695. ISSN: 01968092. DOI: 10.1002/lsm.20573. arXiv: NIHMS150003.

[27] Philippe Lacroute and Marc Levoy. «Fast volume rendering using a shear-warp factorization of the viewing transformation.» In: *Proceedings of the 21st annual conference on Computer graphics and interactive techniques - SIGGRAPH '94*. New York, New York, USA: ACM Press, 1994, pp. 451–458. ISBN: 0897916670. DOI: 10.1145/192161.192283. URL: http://portal.acm.org/citation.cfm?doid=192161.192283.

[28] Haida Liang, Marta Gomez Cid, R. G. Cucu, G. M. Dobre, A. Gh. Podoleanu, Justin Pedro, and David Saunders. «En-face optical coherence tomography - a novel application of non-invasive imaging to art conservation.» In: *Optics Express* 13.16 (2005), p. 6133. ISSN: 1094-4087. DOI: 10.1364/OPEX.13.006133. URL: https://www.osapublishing.org/abstract.cfm?URI=oe-13-16-6133.

[29] Wenchao Liao, Tianyuan Chen, Chengming Wang, Wenxin Zhang, Zhangkai Peng, Xiao Zhang, Shengnan Ai, Deyong Fu, Tieying Zhou, and Ping Xue. «Endoscopic optical coherence tomography with a focus-adjustable probe.» In: *Optics Letters* 42.20 (2017), p. 4040. ISSN: 0146-9592. DOI: 10.1364/OL.42.004040. URL: https://www.osapublishing.org/abstract.cfm?URI=ol-42-20-4040.

[30] Monika Machoy, Julia Seeliger, Liliana Szyszka-Sommerfeld, Robert Koprowski, Tomasz Gedrange, and Krzysztof Woźniak. «The Use of Optical Coherence Tomography in Dental Diagnostics: A State-of-the-Art Review.» In: *Journal of Healthcare Engineering* 2017 (2017). ISSN: 20402309. DOI: 10.1155/2017/7560645.

[31] Mohammad Sultan Mahmud, David W. Cadotte, Barry Vuong, Carry Sun, Timothy W. H. Luk, Adrian Mariampillai, and Victor X. D. Yang. «Review of speckle and phase variance optical coherence tomography to visualize microvascular networks.» In: *Journal of Biomedical Optics* 18.5 (2013), p. 050901. ISSN: 1083-3668. DOI: 10.1117/1.JBO.18.5.050901. URL: http://biomedicaloptics.spiedigitallibrary.org/article.aspx?doi=10.1117/1.JBO.18.5.050901.

[32] MS; Michael R. Hee. «Quantitative Assessment of Macular Edema With Opitcal Coherence Tomography.» In: *Journal of Chemical Information and Modeling* 53.9 (1995), pp. 1689–1699. ISSN: 1098-6596. DOI: 10.1017/CBO9781107415324.004. arXiv: arXiv:1011.1669v3.

[33] Michele Midrio. *Campi Elettromagnetici*. Via Lagrange 3, Padova - 35143: SGE Editoriali, 2006. ISBN: 88-86281-82-X.

[34] T Prykari, J Czajkowski, E Alarousu, and R Myllyla. «Optical coherence tomography as an accurate inspection and quality evaluation technique in paper industry.» In: *Optical Review* 17.3 (2010), pp. 218–222. ISSN: 1340-6000. DOI: 10.1007/s10043-010-0039-y.

[35] Naresh Kumar Ravichandran, Eranga Wijesinghe, Seung-yeol Lee, Muhammad Faizan, Kibeom Park, Hee-young Jung, Mansik Jeon, and Jeehyun Kim. «Swept source optical coherence tomography for in vivo growth monitoring of capsicum annuum seeds treated with different NaCl concentrations.» In: 10323 (2017), pp. 1–4. ISSN: 1996756X. DOI: 10.1117/12.2267457.

[36] M Sabuncu and M Akdogan. «Photonic Imaging with Optical Coherence Tomography for Quality Monitoring in the Poultry Industry: a Preliminary Study.» In: *Revista Brasileira de Ci{ê}ncia Av{í}cola* 17.3 (2015), pp. 319–324.

[37] Marinko V. Sarunic, Michael A. Choma, Changhuei Yang, and Joseph A. Izatt. «Instantaneous complex conjugate resolved spectral domain and swept-source OCT using 3x3 fiber couplers.» In: *Optics Express* 13.3 (2005), p. 957. ISSN: 1094-4087. DOI: 10.1364/OPEX.13.000957. URL: https://www.osapublishing.org/oe/abstract.cfm?uri=oe-13-3-957.

[38] Carlo G. Someda. *Electromagnetic Waves*. 2nd ed. CRC, 2006.

[39] Richard F. Spaide, James M. Klancnik, and Michael J. Cooney. «Retinal Vascular Layers Imaged by Fluorescein Angiography and Optical Coherence Tomography Angiography.» In: *JAMA Ophthalmology* 133.1 (2015), p. 45. ISSN: 2168-6165. DOI: 10.1001/jamaophthalmol.2014.3616. URL: http://archopht.jamanetwork.com/article.aspx?doi=10.1001/jamaophthalmol.2014.3616.

[40] Rong Su, Mikhail Kirillin, Ernest W. Chang, Ekaterina Sergeeva, Seok H. Yun, and Lars Mattsson. «Perspectives of mid-infrared optical coherence tomography for inspection and micrometrology of industrial ceramics.» In: *Optics Express* 22.13 (2014), p. 15804. ISSN: 1094-4087. DOI: 10.1364/OE.22.015804. URL: https://www.osapublishing.org/oe/abstract.cfm?uri=oe-22-13-15804.

[41] Yuankai K. Tao, Mingtao Zhao, and Joseph A. Izatt. «High-speed complex conjugate resolved retinal spectral domain optical coherence tomography using sinusoidal phase modulation.» In: *Optics Letters* 32.20 (2007), p. 2918. ISSN: 0146-9592. DOI: 10.1364/OL.32.002918. URL: https://www.osapublishing.org/abstract.cfm?URI=ol-32-20-2918.

[42] G. J. Tearney, S. A. Boppart, B. E. Bouma, M. E. Brezinski, N. J. Weissman, J. F. Southern, and J. G. Fujimoto. «Scanning single-mode fiber optic catheter–endoscope for optical coherence tomography.» In: *Opt. Lett.* 21.7 (1996), pp. 543–545. DOI: 10.1364/OL.21.000543. URL: http://ol.osa.org/abstract.cfm?URI=ol-21-7-543.

[43] Karin Wiesauer, Michael Pircher, Erich Götzinger, Siegfried Bauer, Rainer Engelke, Gisela Ahrens, Gabi Grützner, Christoph Hitzenberger, and David Stifter. «En-face scanning optical coherence tomography with ultra-high resolution for material investigation.» In: *Optics express* 13.3 (2005), pp. 1015–1024. ISSN: 1094-4087. DOI: 10.1364/OPEX.13.001015.

[44] Wolfgang Wieser, Wolfgang Draxinger, Thomas Klein, Sebastian Karpf, Tom Pfeiffer, and Robert Huber. «High definition live 3D-OCT in vivo: design and evaluation of a 4D OCT engine with 1 GVoxel/s.» In: *Biomed. Opt. Express* 5.9 (2014), pp. 2963–2977. DOI: 10.1364/BOE.5.002963. URL: http://www.osapublishing.org/boe/abstract.cfm?URI=boe-5-9-2963.

[45] Maciej Wojtkowski, Rainer Leitgeb, Andrzej Kowalczyk, Tomasz Bajraszewski, and Adolf F. Fercher. «In vivo human retinal imaging by Fourier domain optical coherence tomography.» In: *Journal of Biomedical Optics* 7.3 (2002), p. 457. ISSN: 10833668. DOI: 10.1117/1.1482379. URL: http://biomedicaloptics.spiedigitallibrary.org/article.aspx?doi=10.1117/1.1482379.

[46] Tuqiang Xie, Huikai Xie, Gary K. Fedder, and Yingtian Pan. «Endoscopic optical coherence tomography with a modified microelectromechanical systems mirror for detection of bladder cancers.» In: *Applied Optics* 42.31 (2003), p. 6422. ISSN: 0003-6935. DOI: 10.1364/AO.42.006422. URL: https://www.osapublishing.org/abstract.cfm?URI=ao-42-31-6422.

[47] Kang Zhang and Jin U. Kang. «Real-time 4D signal processing and visualization using graphics processing unit on a regular nonlinear-k Fourier-domain OCT system.» In: *Opt. Express* 18.11 (2010), pp. 11772–11784. DOI: 10.1364/OE.18.011772. URL: http://www.opticsexpress.org/abstract.cfm?URI=oe-18-11-11772.